Supplementary Information for **Neandertals Made the First Specialized Bone Tools in Europe**

Marie Soressi, Shannon P. McPherron, Michel Lenoir, Tamara Dogandžić, Paul Goldberg, Zenobia Jacobs, Yolaine Maigrot, Naomi Martisius, Christopher E. Miller, William Rendu, Michael P. Richards, Matthew M. Skinner, Teresa E. Steele, Sahra Talamo, and Jean-Pierre Texier

Contents

1 Excavation Methods and Areas Excavated

1.1 Excavation Methods

Pech-de-l'Azé I (Pech I) and Abri Peyrony (AP) were excavated following very similar
protocols. At both sites, stratigraphic unit (i.e. level) designations were based first on
lithological criteria and second on archaeological criteria. All finds were recorded by level.
Three-dimensional coordinates were measured with either Leica or Topcon total stations
connected to data collectors running software (EDM-CE and EDM-Mobile) developed by Dibble
and McPherron (1). All lithics and all fauna larger than 25 mm were given 3D coordinates and a
unique identifier combining the excavation unit with a sequential number (e.g. K16-23).
Complete bones and identifiable teeth smaller than 25 mm (but larger than microfauna) were also
given coordinates and IDs. All natural stones larger than 10 cm were recorded with a single
coordinate, and all natural stones larger than 20 cm were measured with multiple coordinates to
describe their volume and orientation. Natural stones were given a non-numeric, randomly
generated ID (e.g. K16-XXHSX). All sediment, excluding stones larger than 10cm and all other
recorded objects, was collected by 7 liter bucket and wet screened through 2 and 5 mm meshes

thereby creating coarse and fine screen fractions. The fine fraction was archived unsorted. The coarse fraction was sorted to separate fauna, lithics, coprolites and any other items of interest. Buckets typically represent one-quarter of a square meter and a depth of less than 2 cm. All buckets carried a unique ID and the coordinates for the bucket were measured in the center of the area worked at the completion of the bucket. The volume of the bucket was recorded for buckets less than seven liters. Objects that should have been given individual coordinates (i.e. objects > 25 mm) are removed from the coarse fraction, given new identification numbers, and assigned the coordinates of the bucket. In addition to these find records, digital photographs documenting the excavation were recorded daily, and final sections were documented through a combination of photography (sometimes with rectification), drawing, and total station measures. Combustion features and other features were sampled, and their position and morphology were recorded with the total station throughout the excavations.

1.2 Pech-de-l'Azé I Excavations

The sequence exposed in the witness section area consists of ~4 m of very coarse blocks of cliff collapse (dm-sized) and limestone *éboulis* in a clayey sand matrix (Fig. S1 and Fig. 1 in main text). Four main layers were recognized in the recent excavations as well as in previous ones, all attributed to the Mousterian of Acheulian Tradition and forming up to 3 m of deposits. Layer 4 at the bottom of the sequence is attributed to Mousterian of Acheulian Tradition type A. Layers 6 and 7 are attributed to MTA type B (intermediary Layer 5 has a low density of artifacts of both MTA type A and B industries). In 2004, a new Neandertal tooth belonging to another juvenile individual was recovered in Layer 4, thereby confirming the attribution of MTA type A industry to Neandertals (2).
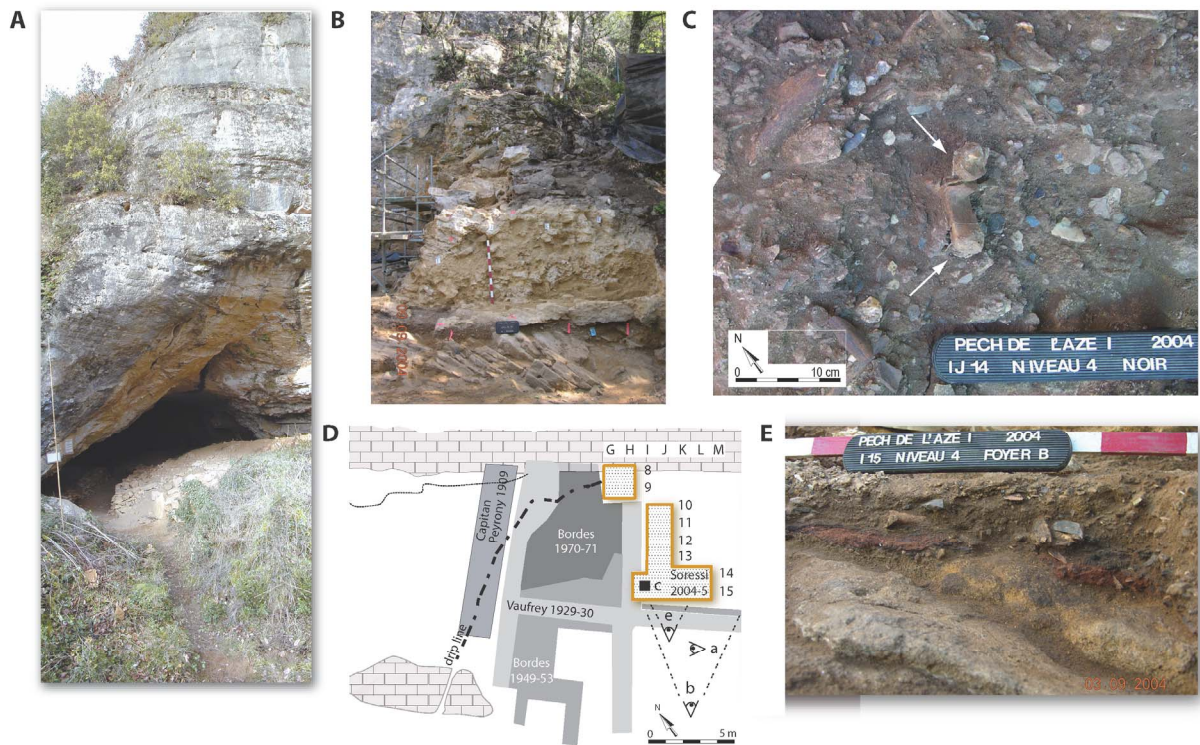
3

Fig. S1. The site of Pech-de-l'Azé I. a, view of the actual porch. b, frontal view of the main witness section excavated in 2004 and 2005. c, upper view of a portion of Layer 4 (squares I-J 14) showing in situ anatomical connections (between a bovid talus and calcaneum). d, map of the successive excavations between 1909 and 2005, showing locations of panels a to e. e, frontal view of a portion of Layer 4 (square I15) showing black and red ashes from fire-places as well as artifacts and bones.

1.3 Abri Peyrony Excavations

In 1990, as part of their excavations at Combe-Capelle Bas, Lenoir and Dibble (3) excavated a 1.5 m² test unit at Abri Peyrony on the lower terrace. In 2009, we (SM and ML) reopened the Lenoir and Dibble excavations and removed backdirt from an adjacent depression dating either to Peyrony's 1925 excavations (4) or to clandestine excavation between 1925 and 1990 (Fig. S2). We then expanded the edges of the depression to have proper sections, excavated the deposits remaining in the depression, and opened a trench across the upper terrace to connect the Lenoir and Dibble unit to the cliff face. This work continued for four weeks in 2010 and again for 2.5 weeks in 2012. Two of the reported bone tools were found during and after the 2010 season, and

the larger, more complete tool was found during the 2012 excavation (Fig. S4). There is no

stratigraphic connection between the upper and lower terrace (Fig. S3). Thus, the stratigraphic

designations contain a prefix to denote whether they come from the lower (L) or upper (U)

terrace. The only layer that connects the two, Layer 1, is backdirt.
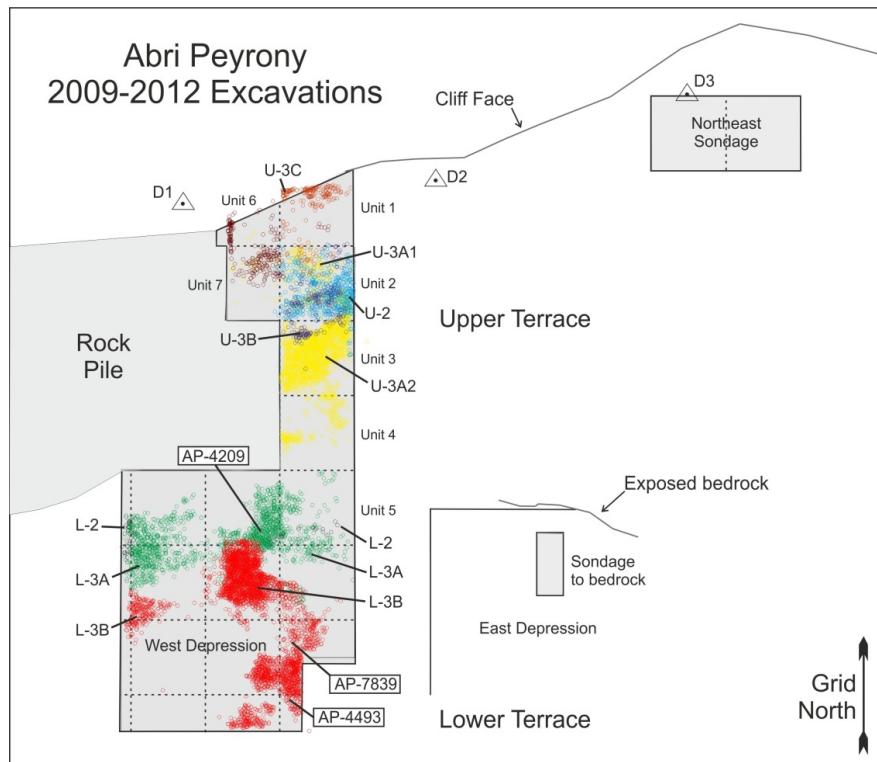
Fig. S2. Excavation units opened at Abri Peyrony. Colored points represent artifacts and buckets
of sediment excavated. The find location of AP-7839 is noted as well as the locations of the
buckets containing AP-4493 and AP-4209.

2   Geology and Site Formation Processes

2.1   Pech-de-l'Azé I Model of site formation

After the first sedimentological analysis undertaken by H. Laville (5), we recently

restudied the complete sequence of Pech-de-l'Azé I. Detailed description and arguments for a

reconstitution of Pech-de-l'Azé I morphogenesis can be found elsewhere (6) . We summarize

here our main results by providing a short geological history for the site.
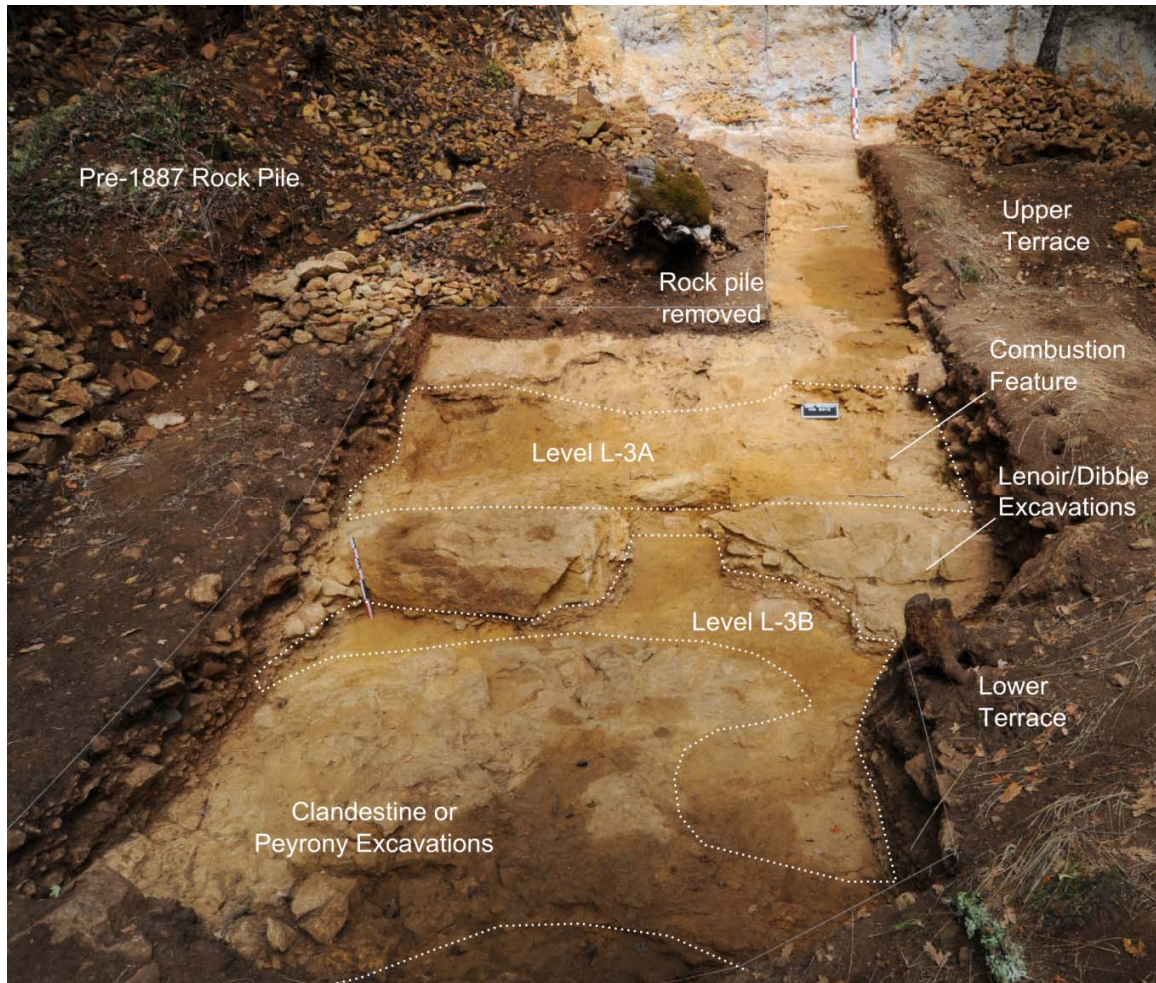
Fig. S3. View (north) of Abri Peyrony after the 2012 excavations. Scale on the left is 40 cm, and the scale at the back is 1 m. Some color variation is due to wetness. The limestone blocks in the center were cut to create the notch in the center of the photograph. A portion of L-3B was sealed below these rocks. The foreground surface is the bedrock of the lower terrace.

A first sedimentary phase occurs in an endokarstic context when the downcutting of Quaternary valleys had just begun. This erosion probably dates to the Lower Pleistocene and lead to the deposition of mainly sandy alluvium. At this time, the karstic passage that links Pech I and II extended far beyond the present entrances. The continuation of the downcutting of the valleys brought about a concomitant slope retreat, which was guided by joints subparallel to the present rock wall. Their N 40° E strike is similar to a well-known structural direction in the Aquitaine Basin (7). During the Middle Pleistocene, the situation at Pech I was probably the one
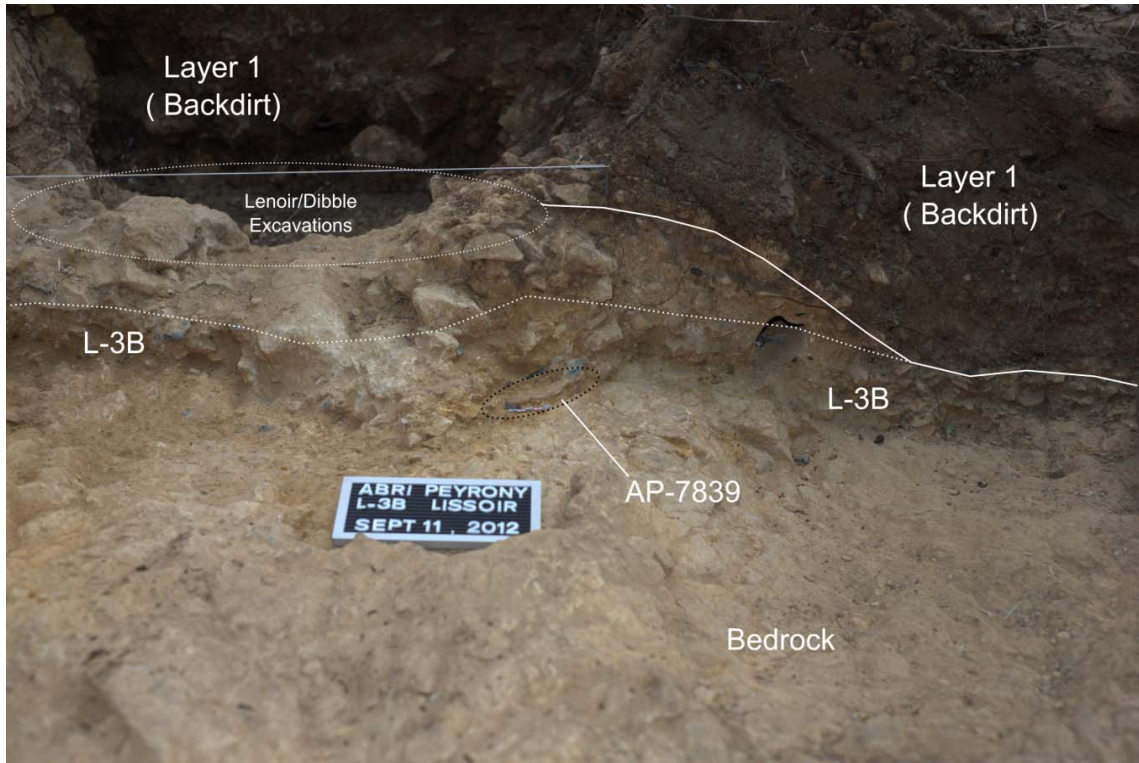
Fig. S4. A portion of the east section of the lower terrace of Abri Peyrony showing AP-7839 in situ. The area to the right and above the solid line (Layer 1) was excavated previously by Peyrony or clandestinely. On the left is the area excavated by Lenoir and Dibble. AP-7839 is centimeters above the bedrock. The scale next to AP-7839 is 5 cm.

indicated on Fig. S5-1. The karstic passage was separated from outside by a rather thin limestone brow. At the beginning of OIS 3, the continuation of this evolution finally leads to the oblique crosscutting of the passage and to the formation of a rockshelter. The first filling phase of the shelter (Fig. S5-2) is contemporaneous with Mousterian of Acheulian Tradition occupations responsible for the formation of archaeological Layers 4 and 5. It is mainly characterized by moderate rockfall processes and by runoff processes, which have resulted in the deposition of sands, reworked from the underlying fluvial deposits. Based on radiometric dating of these layers(8), this episode is situated within OIS 3. Rock fragments associated with the sands are heavily weathered. This suggests that this depositional phase occurred in a rather temperate and humid environment. The next evolutionary phase (Fig. S5-3) takes place just

before the Mousterian occupation of Layer 6. It is expressed by substantial breakdowns of the porch roof. This is revealed by the occurrence of big slabs and boulders visible in the southern part of the site. Acting together with rockfall processes, runoff continues. It carried sands and small gravels that tend to fill in the packing voids between rock-fragments. Next, the retreat and the plugging of the rockshelter continued via the same above-mentioned mechanisms, i.e. rockfall, runoff and percolation. Finally, this morphologic evolution resulted in the entire filling in of the residual shelter and in the slope (Fig. S5-4). It is difficult to date precisely this evolutionary stage to the beginning or the end of OIS 2. During the Holocene, a calcosol or a calcaric rendosol (9) formed on the upper part of this sedimentary series and it has been truncated by the successive excavations that were conducted in the site. The carbonate concretions visible throughout most of the thickness of deposits are related to this pedogenic event.
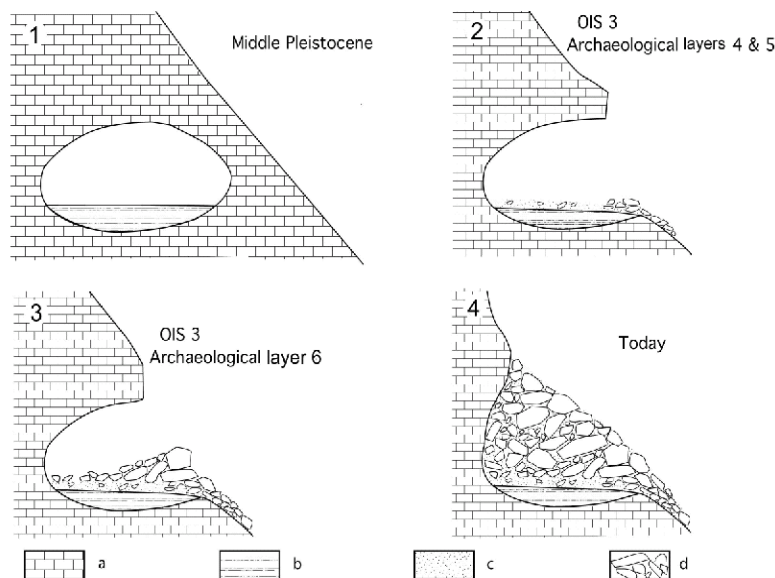

Fig. S5. Main evolutionary stages of Pech-de-l'Azé I. a, Limestone. b, endokarstic fluvial sands. c, sands deposited by runoff and percolation processes. d, pebbles, cobbles and boulders.

The above-described morphogenic evolution permits the extent and the relative richness of the different archaeological layers of Pech to be satisfactorily explained. During the first two

8

Mousterian occupations the shelter is wide and deep. It could accommodate large human groups, and the artifact density is the highest in this layer. Later, during the Layer 6 occupation, the living space decreased. It was less high and deep. Moreover, it was limited in the front by an accumulation of slabs and boulders that may have constituted a natural protection for the occupants. Then, with the increasingly marked retreat and plugging of the shelter, the available space became more and more enclosed. Only small human groups could live there for short stays. This situation prevailed during the formation of archaeological Layer 7.
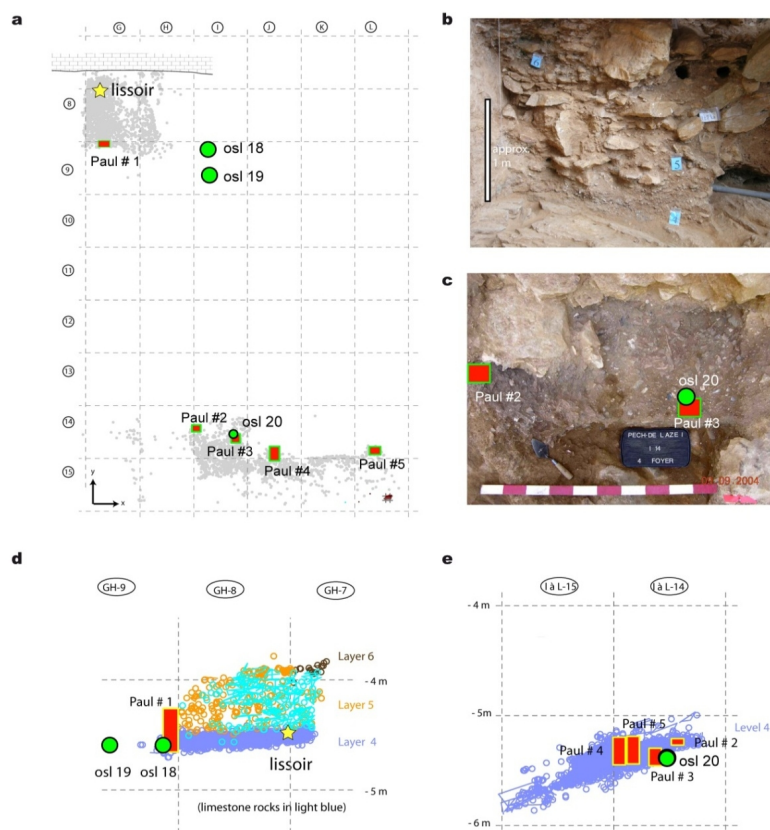
Fig. S6. Location of micromorphological and OSL samples close to the *lissoir* and the combustion features. a, plan view of samples above a profile projection of all 3D recorded finds in Layer 4 during 2004 and 2005 excavation (*lissoir* location is indicated by a yellow star). b, photo of the context of sample Paul # 1. c, photo of samples Paul #2, Paul #3 and OSL 20 before cutting them. d, side view of samples Paul #1, OSL 18 and 19 with 3D recorded finds. e, side view of other micromorphological samples as well as OSL 20 with 3D recorded finds.

9

2.2 Micromorphology of Pech-de-l'Azé I combustion features

The bottom level, Layer 4, which contained the *lissoir*, was sampled for micromorphological analysis, focusing not only on the area were the *lissoir* was found (sample Paul # 1) but also on the combustion features (samples Paul #2 to 5) (Fig. S6).

Layer 4 at the base consists of mostly poorly sorted silty sand that varies in color from light to dark brown, the darker color reflecting the presence of burned material (e.g., charcoal and bone) and organic matter. Combustion features in Layer 4 are expressed as localized red, dark brown, and black layers (see **Error! Reference source not found.**e). In the field, there is no visible evidence of combustion features in the direction of the wall to the north, especially in the recent excavation, which took place ~1 m from the wall.

Sample # 5

Micromorphology sample #5 comes from the eastern portion of layer 4 (see Fig. S6). A scan of the entire ~20 cm-long impregnated block (Fig. S7) shows the bedded nature of this deposit, not only by the orientations of the platy limestone and bone fragments but also by the intact bedding of the dark organic band in the center of the block. It is clear from this photo that vertical movement of objects through the depositional column did not take place.

Fig. S7. Scan of ~20 cm-long block of sample Paul #5 from Layer 4. Note the clear horizontal bedding of the sediment, particularly the orientation of the platy limestone clasts, as well as the intact black organic layer shown by the red arrow. The yellow arrow points to the 'up' direction. The cm scale is at the upper left.

Sample # 4

Two thin sections were examined from micromorphology sample Paul #4 (Fig. S8). The upper part (thin section -4A) is richer in burned bone and is finer grained than the lower part, which is much richer in *éboulis*. Interestingly within the scanned block (shown at left on Fig. S8) a darker zone appears which in hand sample would suggest that this is the remains of an intact feature. In thin section, however, there is very little visible micromorphological evidence for this darkening, although there is possibly a slight enrichment of micro-particles of charcoal or burned bone. The internal geometry of the bone fragments, which exhibit various degrees of burning, mixed with quartz sand and some remains of ash-derived carbonates, show that the burning of these bones took place somewhere else. They could have been moved to their current location by dumping of combusted materials [similar dumping activities can be documented from Kebara Cave in Israel (10)] or are perhaps associated with rake-out of a nearby combustion feature that was accompanied by trampling, as has been observed in the lower layers in nearby Roc de Marsal (11).
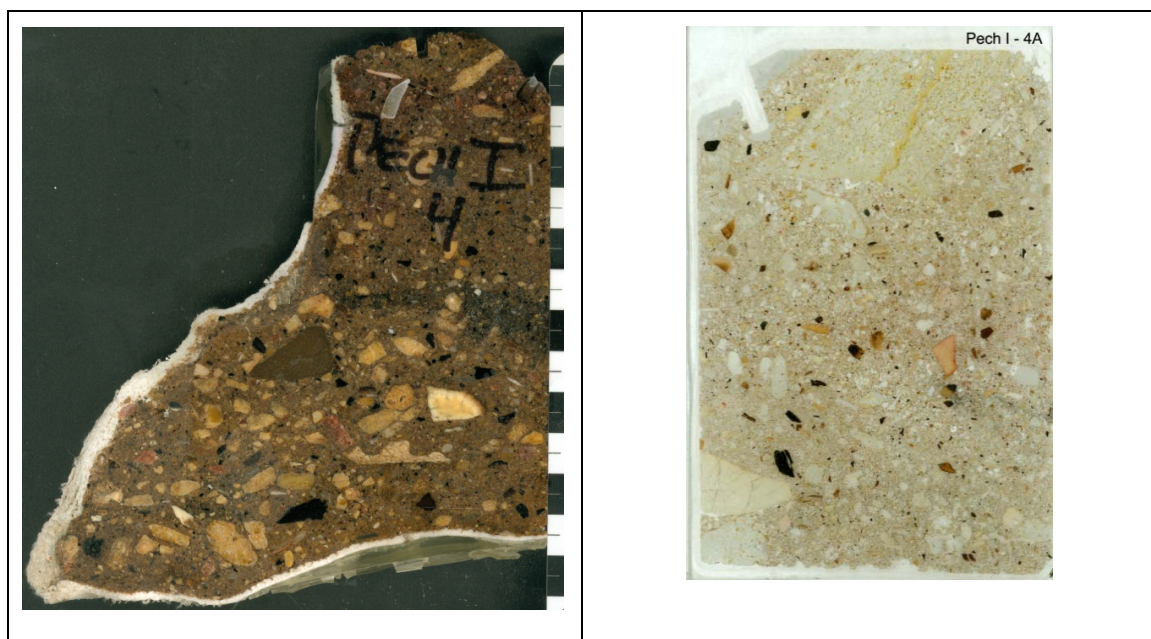
Scan of impregnated block of sample #4 showing two different lithologies separated by a darker band in the middle, which separates a coarser layer at the bottom from a one with fewer cm-sized clasts. The black objects are burned bone. Scale at right is in cm.

Pech I - 4B

Thin section scans of upper and lower parts of sample #4 shown at left. The dimensions of the slides are 50x75 mm.

1 mm
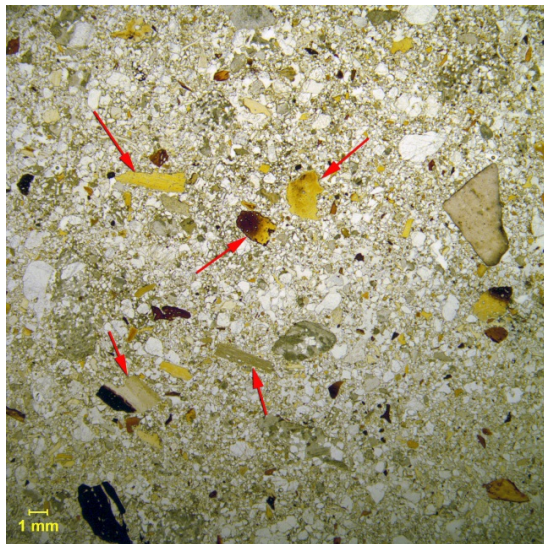
Photomicrograph from the middle part of thin section 4A. Note the different degree of heating of the bone fragments (arrows) scattered throughout. Plane-polarized light (PPL).

1 mm
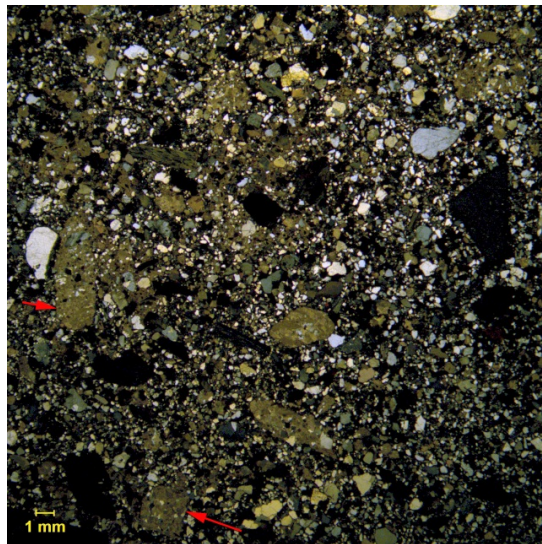
Same as at left but in cross-polarized light (XPL). This material is slightly calcareous, with small amounts of secondary carbonate cementing a silty matrix (arrows).

| Photomicrograph of part of thin section 4B. Bone fragments in the lower and center of the frame are indicated by arrows; a chert flake (c) is also shown. PPL. | XPL view of a different part of section 4B. Circular calcareous root coatings – possibly recent – are shown in the lower part of the slide. |
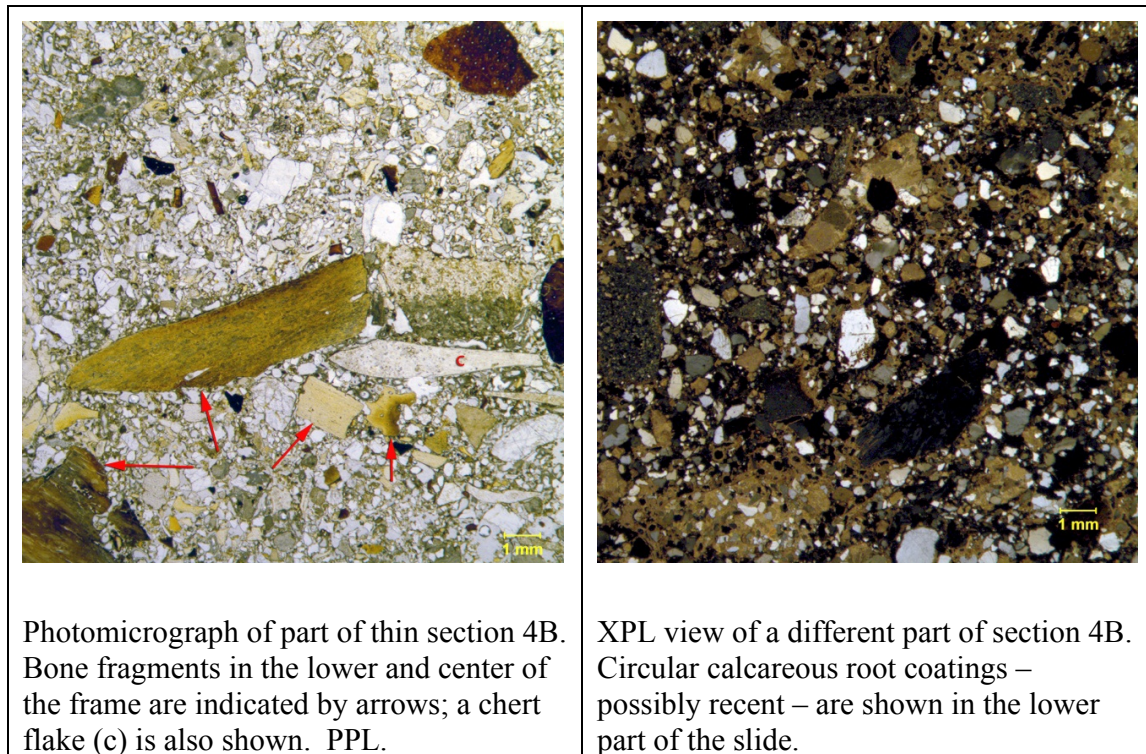
Fig. S8.   Description of micromorphology sample # 4.

The presence of the darker band (possibly slight charcoal enrichment) and the clear difference between the upper and lower parts of the block of sample #4 imply that even though the cultural material (e.g., bones and artifacts) may have been laterally displaced from their original location, no significant vertical post-depositional mixing of these two depositional units was involved; perhaps some trampling occurred, which would displace material on the order of mm or cm. Any movement would have been either the deposition of a new layer or perhaps the accumulation of dumped material containing burnt bone or lateral shifting associated with rake out of previously combusted material. In any case, the burned bones are not in their original position.

Sample # 1

Three thin sections were prepared from the impregnated block of micromorphology sample Paul #1 and include Layer 4 (close to the worked bone location), as well as the bottom of Layer 5. From bottom to top these can be characterized as follows:

Micromorphology sample #1C (bottom of Layer 4) – Sample 1C overall consists of poorly sorted sand composed of mostly quartz, burned and unburned bone, limestone clasts, chert fragments, and some traces of charcoal. The finer grained material is relatively low in abundance and consists of braces of dusty brown clay with localized domains of what appear to be aggregates of silty clay, presumably soil clasts; some of these dark aggregates are suggestive of fine organic matter residua from fires. Post-depositional features include thin reddish brown iron-rich clay coatings, which typically fill intergranular voids; iron staining of bone fragments occurs as thin, discontinuous patches. Carbonate hypocoatings around circular roots are the last diagenetic event, as they clearly post-date the iron and clay movements. Some phosphatization of the limestone grains is also visible.

This part of the sample seems to be remnants of a combustion zone: material is not in place and locally displaced but only on the order of cm, as can be seen in the upper part of the slide, which still exhibits an overall darker color. Displacement of the material is possibly due to trampling, dumping, or rake-out of combusted material, but the original ashes are no longer visible. It does **not** appear that there was large-scale movement of grains or objects (i.e., on the scale of dm or m), as such movements would have destroyed most of the stratigraphic layering visible in the slide.

Micromorphology sample #1B (upper part of Layer 4 in which the worked bone was found and bottom part of Layer 5) – This overlying thin section above 1C exhibits some mm-

sized carnivore coprolite fragments as well as a greater proportion of fine material than in thin section -1C. Finely divided, fine-sand sized charcoal occurs mixed within the matrix, is possibly a result of small-scale (i.e., mm-size) burrowing or trampling.

Micromorphology sample #1A (Layer 5) – This sediment is looser than in the underlying deposits and shows greater effects of biological activity. This activity is expressed by the presence of numerous channels (some with living roots), fine pellets produced by mites (*acarien*), as well as possible earthworm casts. Bones are much less abundant here, as is charcoal.

Layer 5

Layer 4

Pech I - 1A

Pech I - 1B

Pech I - 1C

Scan of thin sections from Micromorphology sample #1. In sample 1C note the scatters of burnt bone throughout the sample particularly in the upper part of the slide. Sample 1B contains some bone and overall is slightly richer in finer matrix material. The uppermost sample, 1A which correspond to Layer 5, shows greater porosity, which is a result of bioturbation likely associated with its being at the top of the sediment column and exposure. Plane-polarized light (PPL); width of all thin section scans is 50 mm.

Micromorphology sample #1C Thin band of organic-rich silts shown by double-ended arrows, with piece of charcoal next to arrow. PPL.
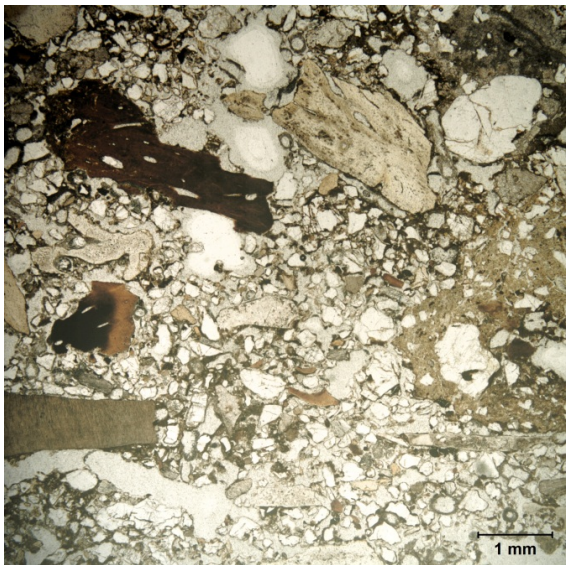
Portion of upper part of thin section 1C, showing mm-size angular bone fragments, most of which are burned but not articulated. At the right is a large clast of silty clay with inclusions of quartz sand. In the upper right hand corner is a clast of limestone. PPL.
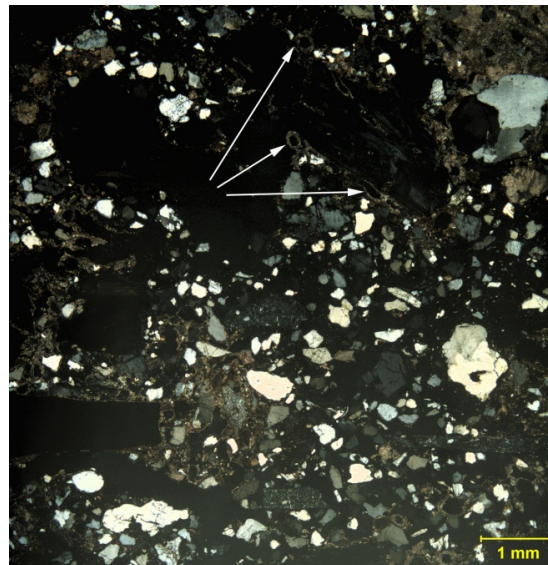
Same as at left but in cross-polarized light (XPL). Arrows point to secondary accumulations of calcite around rootlets.
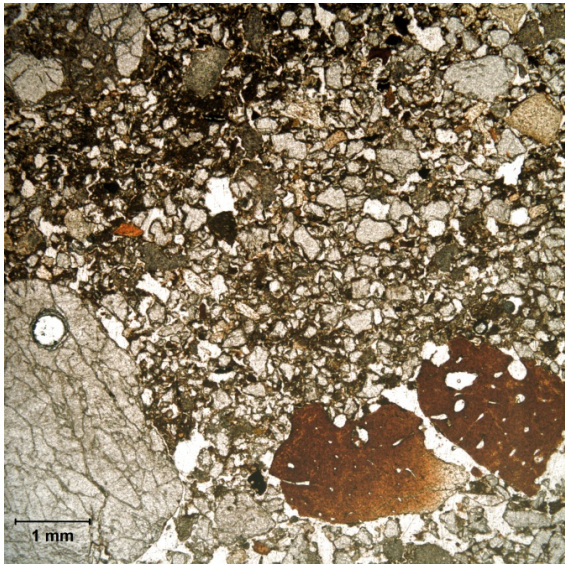
Thin section -1B, showing two rounded, heated bone fragments at the bottom overlain by sand with some iron stained clayey coatings; at the top the amount of interstitial clay increases. PPL.
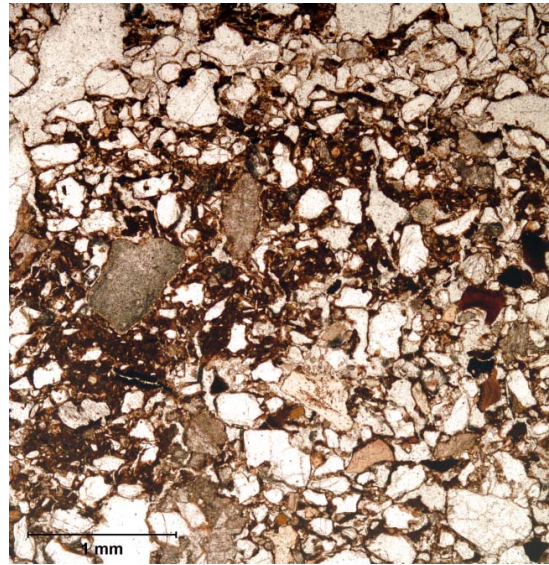
Detail of thin section -1B at left showing silty clay reddish matrix with some inclusions of charcoal and sand size bones; the large grain at center-left is weathered limestone. PPL.
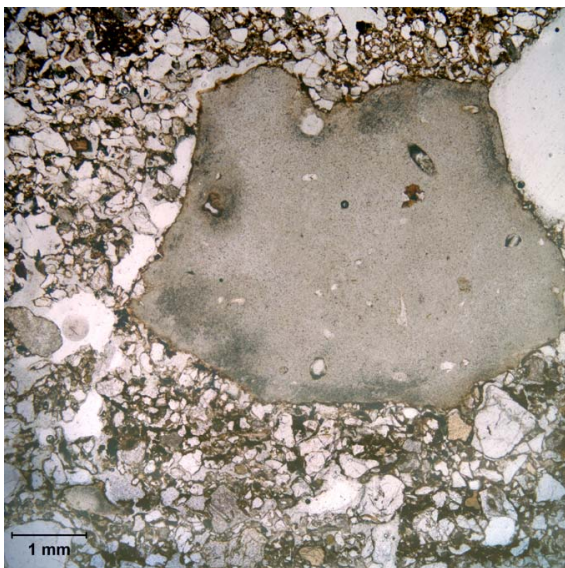
Thin section -1B with granule-size fragment of carnivore coprolite. PPL.

Thin section -1A (Layer 5) showing loose nature of the sediment and biologically-produced aggregates. PPL.

2.3 Pech-de-l'Azé I Summary

Layer 4 artifacts, bones and ashes from fireplaces had been preserved by up to 3 meters of blocks fallen from the limestone walls and roof overhang during Mousterian time. After its last use by MTA type B groups during the formation of Layer 7, the Pech I shelter was considerably reduced and almost non-existent. As a consequence, Layer 4 was preserved from any possible contamination by later Upper Paleolithic excursions to the site.

2.4 Abri Peyrony Geology

The site of Abri Peyrony is located along a cliff and slope of an Upper Cretaceous limestone plateau intersected by the Couze River, a tributary of the Dordogne. The plateau is in turn dissected by two small dry valleys. The cliff face at the top of the plateau, where Abri Peyrony is situated, occurs at the contact between the overlying Maestrichtian limestone, a grainstone containing detrital quartz, fragments of shell and echinoderms, and glauconite within a sparry cement, and the Campanian limestone, a wackestone containing forams and glauconite(12). The Campanian limestone forms a series of benches along the slope of Combe-Capelle, which in turn is overlain by mostly colluvial sediments that contain Middle Paleolithic artifacts. Karstic features are present along the Maestrichtian cliff face, most notably at the nearby site of Roc de Combe-Capelle, where phreatic tubes and arches form the visible remains of a largely collapsed karstic system. Despite the name, Abri Peyrony was probably never a rock shelter in the strictest sense. The lack of evidence for karstic features at the site, compared to those at Roc de Combe-Capelle, and the lack of large collapsed blocks of limestone, suggests that Abri Peyrony was always an open air site, albeit one that abutted a protective cliff face. The presence of artifact-bearing tufa deposits at the base of the cliff face demonstrate that phreatic processes, in the form of ground water seeps, played a role in the formation of the archaeological site.

The current excavations of Abri Peyrony have uncovered significant areas of bedrock, exposing two terraces, an upper and a lower, within the Campanian limestone. The break between the upper and lower terrace occurs about five meters from the cliff face and is associated with a line of rectangular blocks of limestone that run roughly parallel to the break between the two terraces. Where the bedrock has been exposed, yellowish-orange interstitial clayey-silt is present within the cracks of the bedrock, suggesting in situ weathering of the limestone. Due to the break between the two terraces, it is not currently possible to directly correlate the stratigraphic units from one terrace to the other.

The lowest stratigraphic unit excavated within the lower terrace is L-3B. L-3B is situated directly under the fallen blocks of limestone and on the bedrock of the terrace. L-3B is situated below the overlying unit L-3A. L-3B appears in the field as a darker-colored layer with a high density of artifacts. The level is variably cemented by calcite. The upper contact with L-3A is gradual over a few centimeters but is clear.

L-3A appears to be the most extensive behind the line of rectangular blocks at the break in slope between the terraces, although it is difficult to estimate the previous extent of the layer, as it was at least partially removed in the southern part of the site by excavations prior to Lenoir and Dibble. Level L-3A probably corresponds with level AP-2 from the 1990 excavations, described by Lenoir and Dibble (3) as a gray-yellow concreted layer. In the field, L-3A appears as a yellowish layer containing sub-rounded to sub-angular clasts of Maestrichtian limestone within a sandy matrix. The entire layer is cemented by calcite. In micromorphological thin section, the clasts of Maestrichtian limestone are clearly visible and constitute ca. 60-70% of the unit (Fig. S9). The sand between the clasts of limestone consists of angular quartz sand, shell fragments, echinoderm fragments, and glauconite, derived from the erosion of the Maestrichtian

20

cliff face. The entire unit is extensively cemented by two phases of micritic calcite formation.

The first phase of micritic cementation is iron-stained, and probably formed as groundwater,

seeping out of the base of the cliff face, percolated through L-3A. The second phase of micrite

formation takes the form of root hypocoatings, probably formed during a period of stability when

a surface above L-3A was colonized by plants.

Fig. S9. Thin section photomicrographs. a, scan of thin section from contact between L-3A and L-2. L-3A is the lighter-colored unit at the base, and L-2 is the darker-colored unit at the top. Note the sharp, erosional contact and the occurrence of modern roots (MR) and some artifacts, such as burnt bone (BB) within L-2. The thin section is 6 x 9cm. b, photomicrograph of L-2, which is composed of clay-rich matrix with artifacts, such as burnt bone (BB) and also quartz sand (Q). Photo in cross-polarized light. c, photomicrograph of L-3A. Note the clast of sparitic Maestrichtian limestone (ML) within a matrix of micritic calcite. The first phase of calcite formation (C1) is iron stained whereas the root hypocoatings (C2) are not stained. Burnt bone (BB) is also present in L-3A.

Although distinct layering is not visible

within L-3A, a combustion feature was

uncovered within the layer (Fig. S10). In

micromorphological thin section, the combustion

feature appears in primary context and is

composed of a thin (5-8mm) layer of charcoal
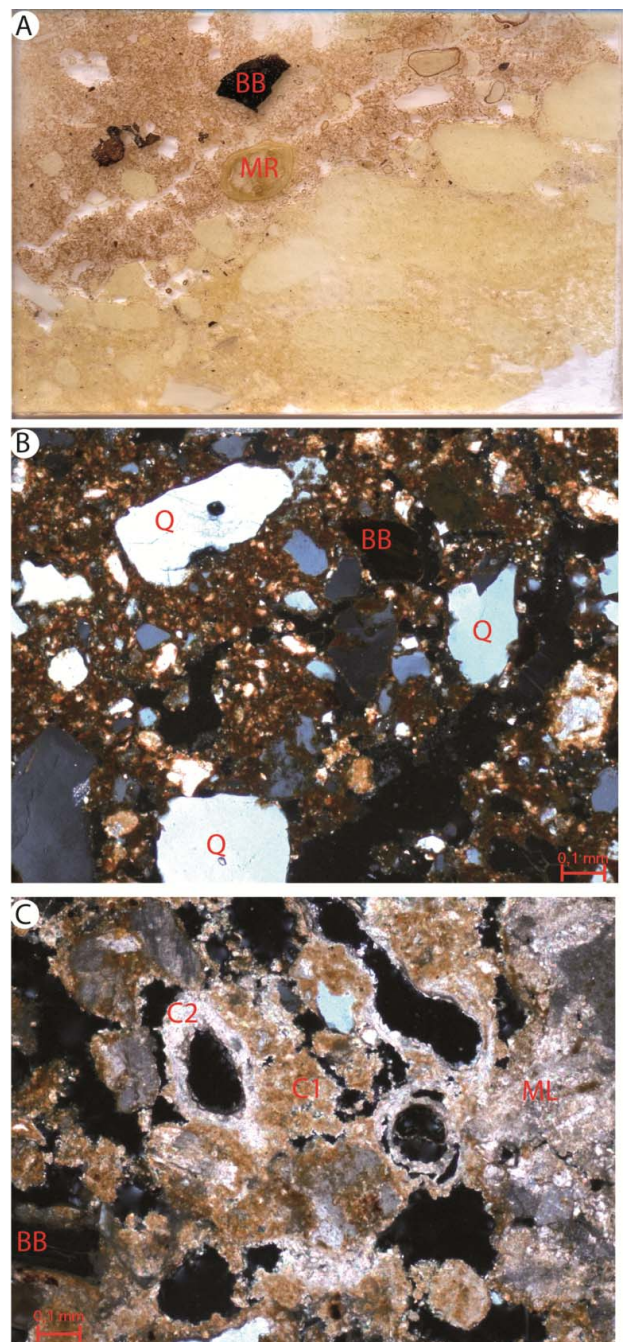
and burnt bone that is locally stained with manganese.
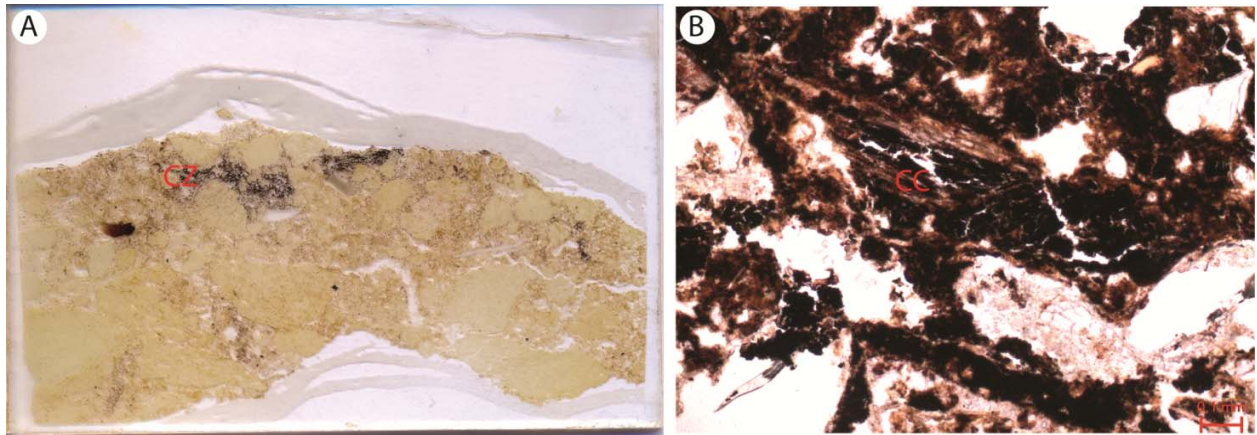
Fig. S10. Thin section and photomicrograph of combustion zone in L-3A. a, Scan of thin section from combustion zone (CZ). b, Photomicrograph from combustion zone within L-3A. Charcoal (CC) and burnt bone are present within the feature. The presence of such a feature suggests that the layers were deposited under low-energy conditions and that the layer has been minimally disturbed by post-depositional processes.

The upper contact of L-3A with L-2 is sharp and appears erosional. L-2 is composed of aggregates of iron-rich clay that incorporate grains of Maestrichtian limestone, angular quartz sand, and artifact-bearing fragments of L-3A. Bioturbation channels are visible, as are modern roots, which run along the sharp surface of L-3A. Some weakly formed pedofeatures, such as clay coatings and infillings, are visible. L-2 probably represents a late Holocene (Medieval-period to early modern) sediment that has incorporated Middle Paleolithic artifacts from the underlying layers. Despite the reworked appearance of L-2, the cementation of L-3A has prevented any significant disturbance of the underlying layers.

The sediment on the upper terrace is thinner than in the lower terrace and appears to exhibit a slight downhill slope. The U-03 layers are strongly cemented and appear at least locally to exhibit laminar structures. These laminar tufa deposits are particularly well developed along the edge of the cliff face, from where ground water periodically seeped. The overlying U-

02 layers appear more reddish in color, compared to the yellowish, cemented layers of U-03 and resemble L-2, possibly suggesting that U-2 is at least partially reworked.

2.5 Abri Peyrony Model of site formation

The initial occupation of the site corresponds with layer L-3B that is rich in artifacts and burnt material, giving the sediment its dark color. Following the formation of these initial layers, a rock fall from the Maestrichtian cliff line partially sealed these layers. L-3A formed shortly after this small rock fall event as a result of erosion from the backing cliff. The clastic sediment of L-3A is composed exclusively of material derived from the Maestrichtian limestone, including sub-angular clasts of the limestone and sand-sized components, such as quartz grains, echinoderm fragments and glauconite, which were deposited as a result of disaggregation of the limestone cliff. The lack of soil or clay aggregates suggest that the sole sediment source for L-3A was the limestone cliff, and not any type of sediment or soil located on the plateau. Although distinct layers and sedimentary structures are absent from L-3A, the preservation of a combustion feature within the layer suggests that the accumulation of the sediment for this layer occurred under low-energy conditions. During, or shortly after, deposition of L-3A, ground water seeps, as evident by the occurrence of tufa deposits along the backing cliff line of the site, cemented the deposit. Although the laminated appearance of the tufa deposits in the upper terrace suggest some weak sheet flow, the cementation of L-3A occurred as a result of repeated percolation of water moving through the deposit. This type of repeated percolation accounts for the micritic appearance of the secondary interstitial calcite, and also for the iron staining of the calcite. The tufa deposits can be traced across the cliff line and is also present at Roc de Combe-Capelle. The ground water seep probably did not occur simultaneously along the cliff line, but occurred sporadically at different localities, eventually building up a wide sheet of tufa along the

cliff. The ground water seep appears to be no longer active, suggesting that the formation of this tufa was associated with different past environmental conditions, possibly wetter than today.

Once the groundwater seep ceased, the surface of L-3A was colonized by plants, whose roots penetrated the deposit. As the roots took up water, they caused dissolved calcite to crystallize around the roots, creating the second phase of calcite formation within L-3A. Eventually the cemented surface was at least partially eroded, although it is difficult to determine how much material was ever removed. The cemented surface was then eventually buried under Holocene deposits, potentially derived from the plateau behind the cliff face.

2.6 Abri Peyrony Summary

The geoarchaeological investigation at Abri Peyrony demonstrates that the site preserves low-energy deposits that were largely not influenced by significant post-depositional disturbance. The preservation of an intact combustion feature within L-3A suggests that the layer was not subject to significant high-energy depositional processes, but rather formed as a gradual accumulation of detrital material derived from the Maestrichtian limestone cliff. Although laminar tufa deposits within the upper terrace may have provided some energy to partially displace artifacts, the effects of the groundwater seep within the lower terrace was limited to percolation through the deposit. In fact, it is this percolation and cementation that accounts for the preservation of the archaeological site. The cementation was so thorough that modern roots are not capable of breaking through. Therefore, L-3A and the underlying L-3B deposit are intact and represent sealed contexts.

2.7 Methods for micromorphological samples (Pech I and Abri Peyrony)

Intact blocks of sediment were removed using plaster jackets from excavated portions of both sites. The blocks were transported either to the MicroStratigraphy Laboratory at Boston

University (Pech I samples) or to the *Institut für Naturwissenschaftliche Archäologie* at the University of Tübingen (Abri Peyrony samples). Samples were dried at 60°C for several days and then the blocks were impregnated with an unpromoted polyester resin, which was diluted with styrene at a ratio of 7 parts resin to 3 parts styrene. Methyl ethyl ketone peroxide (MEKP) was used as the catalyzing agent (3-5ml MEKP per liter of resin/styrene mixture). Abri Peyrony samples were placed in a vacuum chamber for 30 minutes to facilitate the impregnation of the samples. For both sites, after curing for a week, the samples were again heated to 60°C overnight to fully polymerize the resin. The samples were then cut into 75mm x 50 mm sized-blocks and sent to Spectrum Petrographics (Vancouver, Washington, USA), where they were made into thin sections. The thin sections were analyzed using a petrographic microscope (Nikon Optiphot2 for Pech I samples, and Zeiss AxioImager for AP samples) in plane-polarized light (PPL), cross-polarized light (XPL), oblique incident light (OIL), and with blue light fluorescence. Observations are made at magnifications varying from 0 to 200x; descriptions follow the guidelines of Stoops (13) and Courty et al. (14).

3   OSL and AMS Dating

3.1 Pech-de-l'Azé I Previous Dates

Previous numerical dating of the site using a combination of several techniques (AMS ^{14}C, Uranium-series, and electron spin resonance (ESR)) showed that the top of the sequence (Layers 6 and 7) is likely to be 40 ± 2 ka (mean early uptake (EU) ESR age for Layer 6) or older (8). The wide spread in ESR/U-series ages resulted mainly from uncertainties in the gamma-dose rate which could not be estimated from the exact location from which each individual tooth sample was collected. Most samples were taken from museum collections and from areas of the excavation for which the sediments have been removed. ESR/U-series ages for the lowermost Layer 4 (in which the *lissoir* was discovered) were not reported in (*4*), but the mean EU-ESR age

of 49 ± 6 ka for the overlying Layer 5 can be taken as a probable minimum age for Layer 4, by the principle of superposition. A conventional ^{14}C age was, however, obtained for Layer 4 in the early 1970s by W. Mook. The age was 42.23 ±1.34 ka ^{14}C BP (GrN 6784) and would correspond to a calibrated age of 46930 to 44470 calBP (68.2%) using IntCal09 calibration curve (15). This age is considered as a minimum age as it was done on two kilograms of burnt bone. New OSL ages obtained for three sediment samples collected from Layer 4 are detailed below. These age estimates confirm the minimum ages previously obtained and provide a weighted mean age of 51.4 ± 2.0 ka (P=0.89) as best age estimate for deposition of the sediments into which the pene-contemporaneous archaeological remains, including the *lissoir*, are found.

3.2 Pech-de-l'Azé I Optically stimulated luminescence (OSL) dating

OSL dating provides a means of determining burial ages for sediments (16–21). The method is based on the increase in number of trapped electrons in mineral grains (such as quartz) with increasing time after burial, in response to the energy supplied by background levels of ionizing radiation from environmental sources. The time elapsed since sediments were last exposed to sufficient heat or sunlight to empty the relevant electron traps can be estimated from measurements of the OSL signal, together with determinations of the radioactivity of the sample and the material surrounding it to a distance of ~50 cm. The burial dose ('equivalent dose', D_e) can be measured using the OSL signal from a sample of sediment, which can be as small as a single sand-sized grain, and represents the radiation dose to which sedimentary grains have been exposed in their burial environment. The dose rate (D_r) represents the rate of exposure of these grains to ionizing radiation over the entire period of burial; this dose is mostly derived from the radioactive decay of ^{238}U, ^{235}U, ^{232}Th (and their daughter products) and ^{40}K, with lesser contributions from cosmic rays and from radioactive inclusions internal to the dated mineral

26

grains. The burial age of grains that were well bleached by sunlight at the time of deposition can then be calculated from the D_e divided by the D_r.

3.2.1 Sample collection and preparation

We collected three sediment samples from Layer 4 from two different areas during July, 2011. The first two samples (PdLI-18 and PdLI-19) were collected from the east face of the Soressi excavation in Square I9 and the other sample in the north face and in the indentation left by micromorphology sample Paul #4 in Square I14 of the Soressi excavation (Fig. S4a, d, and e).

All samples were collected at night using a red-filtered light to ensure that sediments were collected from a single layer. This approach was necessary because of the high frequency of rocks that made sample collection with tubes problematic. Also, the sediments were partly cemented and difficult to penetrate with a tube. Sediments were removed using a small hand trowel and placed in a zip-lock plastic bag that was then subsequently sealed in light-safe black plastic bags and transported to the laboratory. A sub-sample was also collected at each sample position for soil moisture content and laboratory-based radioactivity measurements.

The location of samples PdLI-18 and 19 were determined by the location of two previously made large holes for gamma spectrometry by Rink in 1999/2000. There are not a lot of sediments left at Pech I, so to preserve as much of the deposit as possible, but still being able to make the required *in situ* gamma spectrometry measurements, we collected these two samples inside and adjacent to the two Rink gamma spectrometry holes, and we did our own gamma spectrometry measurements inside these same holes. This allowed us to check the consistency of the gamma dose rate measurements conducted by two different laboratories more than a decade apart, and it also gave us the estimate of the gamma dose rate at the point of sampling.

In the OSL dating laboratory at the University of Wollongong, the sample bags were opened under dim red light. Quartz grains were then extracted using standard preparation procedures (17, 22). First, carbonates were dissolved in 10% hydrochloric acid and then organic matter was oxidized in 30% hydrogen peroxide solution. The remaining sample was dried and then sieved to isolate grains of 90-125 and 180-212 μm in diameter, and feldspar, quartz and heavy minerals were separated by density separation using sodium polytungstate solutions of 2.62 and 2.70 specific gravities, respectively, for each grain-size fraction. The separated quartz grains were etched with 48% hydrofluoric acid for 40 minutes to remove the alpha-irradiated rind of each quartz grain and to destroy any remaining feldspars, and then rinsed in hydrochloric acid to remove any precipitated fluorides, dried and sieved again; grains retained on the 180 μm diameter mesh were used for dating.

3.2.2 Equivalent dose (De) determination

D_e values were estimated for individual 180-212 μm in diameter sand-sized grains from all three samples. We used the standard Risø single grain aluminum discs (23) for measurement of all individual grains, and we confirmed the presence of only one grain in each hole after measurement by systematically checking the discs under a microscope.

All measurements were made in an identical manner and with the same equipment, using the single aliquot regenerative-dose (SAR) procedure described elsewhere (e.g., (24)). The SAR procedure involves measuring the OSL signals from the natural (burial) dose and from a series of regenerative doses (given in the laboratory by means of a calibrated ^{90}Sr/^{90}Y beta source), each of which was preheated at 180°C for 10 s prior to optical stimulation by an intense, green (532 nm) laser beam for 2 s at 125°C. The resulting ultraviolet OSL emissions were detected by an Electron Tubes Ltd 9235QA photomultiplier tube fitted with Hoya U-340 filters.

A fixed test dose (~10 Gy, preheated at 180°C for 5 s) was given after each natural and regenerative dose, and the induced OSL signals were used to correct for any sensitivity changes during the SAR sequence. A duplicate regenerative dose was included in the procedure, to check on the adequacy of this sensitivity correction, and a 'zero dose' measurement was made to monitor the extent of any 'recuperation' induced by the 180°C preheat. As a check on possible contamination of the etched quartz grains by feldspar inclusions, we also applied the OSL IR depletion-ratio test (25) to each grain at the end of the SAR sequence, using an infrared exposure of 40 s at 50°C.

The D_e values were estimated from the first 0.22 s of OSL decay, with the mean count recorded over the last 0.3 s being subtracted as background. Example OSL decay curves for a dim, medium and bright single grain are presented in Fig. S 11a-c for sample PdLI-20. We have checked for the sensitivity of the D_e values to changes in signal integration time and to the use of an early background subtraction (e.g., (26)), but observed no significant changes and preferred the systematic application of the same signal and background integration range applied to each grain. The dose-response data were fitted using a saturating exponential or saturating exponential plus linear function, and the sensitivity-corrected natural OSL signal was projected on to the fitted dose-response curve to obtain the D_e by interpolation. Example dose response curves for the same dim, medium and bright single grains presented for each sample in Fig. S 11a-c are also shown as inset plots. The uncertainty on the D_e estimate of each grain (from photon counting statistics, curve fitting uncertainties, and an allowance of 2% per OSL measurement for instrument irreproducibility) was determined by Monte Carlo simulation, using the procedures described by Duller (27) and implemented in Analyst version 3.24. The final age uncertainty includes a further 2% (added in quadrature) to allow for any bias in the beta source calibration.

The ^{90}Sr/^{90}Y beta source was calibrated using a range of known gamma-irradiated quartz standards for both multi-grain aliquots and individual grain positions. Spatial variations in beta dose rate for individual grain positions were taken into account, based on measurements made using the same gamma-irradiated quartz standards (e.g., (28)).

Aberrant grains were rejected using the quality-assurance criteria described and tested previously (29). Grains were rejected if they exhibited one or more of the following properties: 1) weak test-dose OSL signals (i.e., the initial intensity of the test-dose signal was less than three times the background intensity); 2) high levels of recuperation (i.e., the sensitivity-corrected OSL intensity measured in the 0 Gy regenerative-dose cycle was more than 5% of the sensitivity-corrected natural OSL intensity); 3) poor recycling ratios (i.e., the sensitivity-corrected OSL values for duplicate regenerative doses differed by more than 2σ); 4) natural OSL signals equal to or greater than the saturation limit of the dose-response curve (i.e., the sensitivity-corrected natural OSL intensity exceeded that induced by the largest regenerative dose ('Class 3' grains of Yoshida et al., 2000) or lay in the saturated region of the dose-response curve, so a finite estimate of D_e could not be obtained); and 5) significant loss of OSL signal after exposure to infrared stimulation (i.e., the OSL IR depletion ratio was less than unity by more than 2σ, which indicates
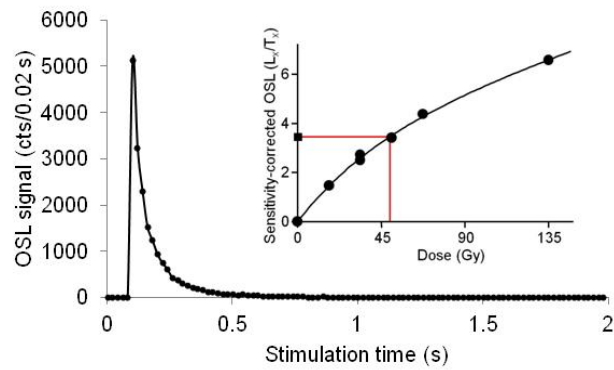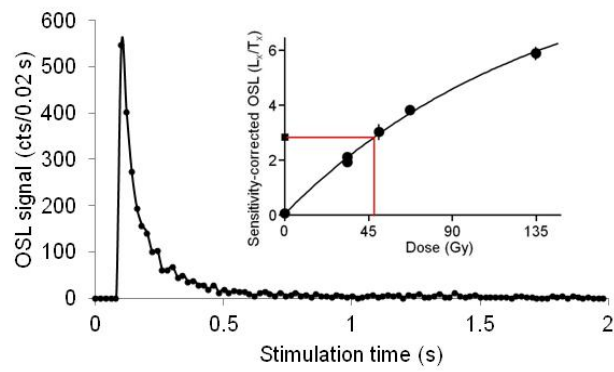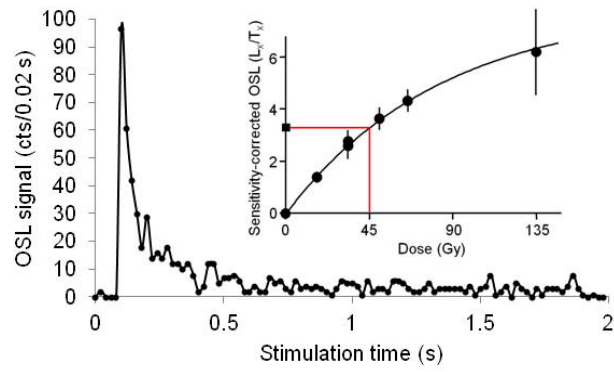
Fig. S 11a-c. Decay curves and dose response curves for representative dim, medium and bright individual grains from sample PdLI-20.

Table S1. Number of single-grains measured, rejected and accepted, together with the reasons for their rejection.

Sample name	No. of grains measured	T_N signal <3xBG	0 Gy dose >5% of L_N	Poor recycling ratio	No L_N/T_N intersection	Depletion by IR	Sum of rejected grains	Acceptable individual D_e values
PdLI-18	2000	1603	55	98	41	113	1910	90
PdLI-19	1900	1475	59	94	25	121	1774	126
PdLI-20	2000	1590	57	108	6	99	1860	140

T_N is the OSL signal measured in response to the test dose given after measurement of the natural OSL signal.
L_N is the natural OSL signal.
Recycling ratio is the ratio of the sensitivity-corrected OSL signals measured from duplicate doses to test the efficacy of the test dose correction used in the SAR procedure.
IR is the infrared stimulation used to erase any part of the signal that may be derived from IR-sensitive (e.g., feldspar) grains.

contamination of quartz grains by feldspar inclusions). Table S1 provides the details for all three samples and the reasons for why single grains were rejected.

Under these experimental conditions, and using these quality-assurance criteria, we recovered correct dose estimates for single grains of quartz from PdLI-20 that had first been bleached with natural sunlight for 4 days and then given a known dose of 60 Gy in the laboratory. The mean ratios of measured to given dose (0.97 ± 0.02, n = 104) are statistically consistent with unity, which shows that the chosen SAR procedures can accurately recover a known dose under controlled conditions. An overdispersion (OD) value of 7 ± 2% was obtained for this dose recovery data set. Such values are similar to those reported previously for dose recovery tests (e.g., (30)). Overdispersion refers to the relative spread in the dose distribution above and beyond that associated with the measurement uncertainties of individual grains, and

was calculated using the Central Age Model (31). If all of the scatter were due to measurement error alone, then the OD value would be zero.

3.2.3 Equivalent dose (De) results

Of the 5900 individual grains measured, only 356 grains (6.0%) were used for final D_e determination. Reasons for rejecting individual grains are provided in Table S1. The majority of grains (79.2%) were rejected because they were too dim following a laboratory dose (T_N signal<3xBG). It is common in studies of quartz grains from a range of geographic and depositional environments that a large proportion of measured grains are not luminescent (e.g., (32)). The D_e values for the accepted grains are displayed as radial plots in Fig. S12a-c, for each of the samples. The single grain D_e distributions are spread only slightly more widely than can be explain by measurement uncertainties alone. The single-grain D_e distributions are overdispersed by between 16 ± 2 (PdLI-20) and $18 \pm 3\%$ (PdLI-18) (Table S1). This degree of overdispersion is typical of samples, measured from around the world, that are considered to be well-bleached prior to deposition, and that remained undisturbed since burial. The D_e distribution patterns when displayed as radial plots (Fig. S12), also support this interpretation (i.e., there are no clear patterning or discrete dose components that may suggest partial bleaching, post-depositional mixing or large-scale differences in the beta dose received by individual grains; (20)). Furthermore, the lack of post-depositional mixing also concurs with the evidence from the soil micromorphology that indicate no vertical movement of objects through the deposits (see Section 3.2).

As a result, we used the central age model (CAM) of Galbraith et al. (31) to combine the single-grain D_e values meaningfully in order to obtain the most accurate estimate of D_e for age

a. PdLI-18
N = 90
OD = 17 ± 3%

b. PdLI-19
N = 126
OD = 18 ± 3%

c. PdLI-20
N = 140
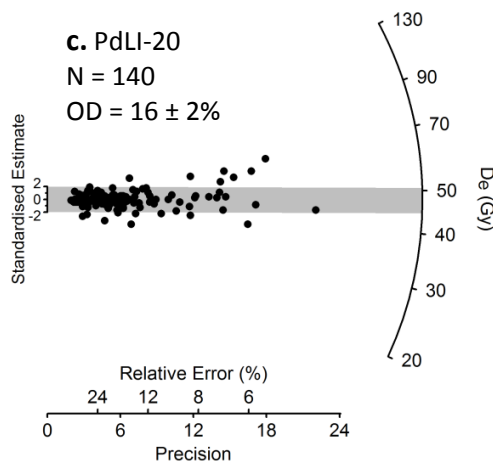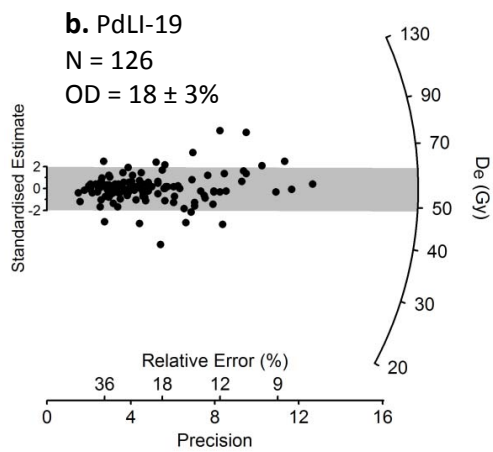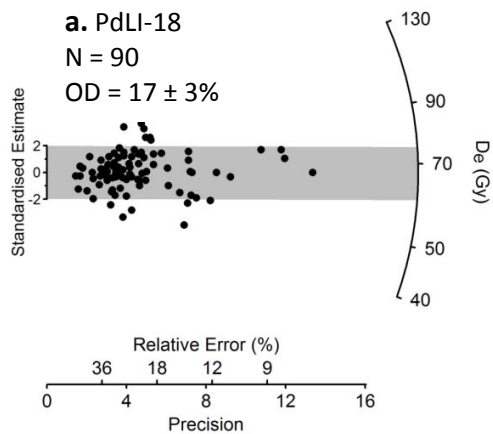OD = 16 ± 2%

Fig. S12a-c. Radial plots of single-grain D_e distributions for OSL samples from Layer 4 at Pech 1. If the D_e estimates in each distribution were statistically consistent (at 2σ) with a common value, then 95% of the points should fall within any grey band projecting ± 2 units from the standardized estimate axis. The grey band is centered on the CAM weighted mean D_e value.

calculation. The CAM model assumes that the D_e values for all grains are centered on some average value of D_e (similar to the median) and the estimated standard error takes account of any overdispersion (31). Information about the number of grains measured and used, overdispersion values calculated and the final $D_e \pm 1\sigma$ value for each sample is presented in Table S2.

Table S2. Dose rate data, equivalent doses and OSL ages for sediment samples from Layer for at Pech de l'Aze I.

Sample code	Moisture content (%)	Dose rates (Gy/ka)			Total dose rate (Gy/ka)	D_e (Gy)	Number of grains	Over-dispersion (%)	Optical age (ka)
		Beta	Gamma	Cosmic					
PdLI-18	4.0	0.54 ± 0.03	0.63 ± 0.03	0.08	1.28 ± 0.07	67.6 ± 2.1	90 / 2000	17 ± 3	52.7 ± 3.5
PdLI-19	3.6	0.47 ± 0.03	0.52 ± 0.03	0.08	1.10 ± 0.06	55.4 ± 1.4	126 / 1900	18 ± 3	50.6 ± 3.2
PdLI-20	4.0	0.39 ± 0.03	0.36 ± 0.02	0.16	0.95 ± 0.05	48.4 ± 1.0	140 / 2000	16 ± 2	51.1 ± 3.1
								Weighted mean =	**51.4 ± 2.0 (*P*=0.89)**

3.2.4 Dose rate determination and results

The total dose rate consists of contributions from beta, gamma and cosmic radiation external to the grains, plus a small alpha dose rate due to the radioactive decay of U and Th inclusions inside sand-sized grains of quartz. To calculate the OSL ages, we have assumed that the measured radionuclide activities and dose rates have prevailed throughout the period of sample burial.

An internal alpha dose rate of 0.032 ± 0.01 Gy/ka has been assumed for all samples.

Beta dose rates were measured directly by low-level beta counting of dried, homogenized and powdered sediment samples in the laboratory, using a GM-25-5 multi-counter system (33). There is no practicable way to obtain an estimate of the external beta dose rate specific to each of the measured individual grains, but based on the D_e distribution for the samples from Pech I (Fig. S11), it would appear that these grains were not exposed to widely varying beta dose rates, and that this estimate of the average beta dose rate for the bulk sample is appropriate. For all samples, allowance was made for the effect of sample moisture content (34), as well as grain size

(35) and hydrofluoric acid etching (36) on beta-dose attenuation, and a systematic uncertainty of 3% was included in the standard error to the beta dose rate.

Gamma dose rates were measured at each sample location by *in situ* gamma spectrometry, to take account of any spatial heterogeneity in the gamma radiation field within 30 cm of each OSL sample (as gamma rays can penetrate this distance through sediment and rock). Counts were collected for 60 min with a 2-inch Na(Tl) crystal. The detector was calibrated using the concrete blocks at Oxford (37) and the gamma dose rate was determined using the 'threshold' technique (38). This approach gives an estimate of the combined dose rate from gamma-ray emitters in the U and Th chains and from ^{40}K. We assigned a relative uncertainty of 5% (at 1σ) to each estimate of the gamma dose rate. We compared our estimates of the gamma dose rate for sample PdLI-18 and PdLI-19 with those of Jones (39) obtained for the same holes. We obtained almost exactly the same gamma dose rate estimates; for PdLI-18 (Gamma7 of (39)) we obtained 0.640 Gy/ka compared to their estimate of 0.654 Gy/ka and for PdLI-19 (Gamma6) we obtained an estimate of 0.524 Gy/ka compared to 0.490 Gy/ka. This is great consistency between different laboratories, but what is interesting is the significant difference in gamma dose rate between the two samples that were collected from positions only ~50 cm apart. Such variations may proof problematic when the gamma dose rate has to be reconstructed for stone or tooth samples that were collected from museum collections and for which an average estimate would be used for estimation of age. This is one of the advantages of OSL dating of sediment where the gamma dose rate can be determined in the field at the point of sampling.

Account was also taken of the cosmic-ray contribution, which was adjusted for site altitude (~165 m), geomagnetic latitude (47.3°), the density and thickness of rock and sediment overburden (40), and the $\cos^2$-Φ zenith angle dependence of cosmic rays (41). We also took into

account the morphological evolution of the cave as illustrated in Fig. S5. We assigned a relative uncertainty of 10% to account for the systematic uncertainty in the primary cosmic-ray intensity (40).

The beta, gamma and cosmic-ray dose rates were corrected for long-term water contents. We used a value of 5%, that is similar to the current measured field values that ranged between 3.6 and 4.2% (Table S2). A relative uncertainty of ±25% (at 1σ) was assigned to each estimate of water content to accommodate any likely variations over the burial period (see Table S1). The value of 5% is lower than the 10% used in the ESR dating study of Soressi et al. (8); they used 10%. As a general rule, the total dose rate will decrease, and the OSL age will increase, by ~1% for each 1% increase in water content. For the three samples presented in this study, this will result in an increase in the age of less than the 1σ error margin.

3.2.5 OSL ages

The D_e values and dose rate information are presented in Table S2, together with the OSL ages for all three samples. Three features of the OSL chronology for the samples collected from Layer 4 in Pech I, and dated here, are noteworthy. First, there is good reproducibility of OSL ages *within* Layer 4. Second, a statistical (chi-squared) test of age homogeneity (based on (42)) indicates that the ages for Layer 4 are statistically consistent with a common true age, which can be represented by a weighted mean age estimate of 51.4 ± 2.0 ka (*P*=0.89). Third, the OSL ages obtained for Layer 4 are consistent with expectations based on the electron spin resonance (ESR), radiocarbon (^{14}C) and coupled U-series/ESR age estimates for the overlying layers (see (8)).

3.3   Abri Peyrony AMS dates

3.3.1   14C Method

The chronology of Abri Peyrony site is based on radiocarbon dating of human modified bones. Seven bone samples with cut marks from Levels L-3A and L-3B were pretreated at the Max Planck Institute (MPI) for Evolutionary Anthropology (Leipzig, Germany) following the method established in Talamo & Richards (43) and as described below. Subsequently, the extracted collagen was sent to the Klaus-Tschira-AMS facility of the Curt-Engelhorn Centre, Mannheim, Germany, for AMS dating. Note that at the time the analysis was conducted, bone samples from L-3C were not yet available for sampling.

Bone samples are cleaned by sand-blasting and 500 mg of whole bone is taken. The samples are decalcified by keeping them in 0.5M HCl at room temperature until no CO_2 effervescence is observed. A step with 0.1M NaOH is added to remove humics, followed by further rinsing with 0.5M HCl. The gelatinization step is done following Longin (44), at pH3 in a heater block at 75°C for 20h. The gelatine is filtered in an Eeze-Filter™' (Elkay Laboratory Products (UK) Ltd.) to remove mineral particles. An ultrafiltration step is applied to all the gelatine samples using Sartorius "Vivaspin 15" of 30 KDalton size filters (45, 46). The samples are lyophilized for 48 hours.

3.3.2   Results

The collagen extract is weighed into pre-cleaned tin capsules for stable isotopic analysis. Before sending the samples to an AMS facility, we routinely check the preservation of the bone collagen using the C:N ratio, $\delta^{13}C$ and $\delta^{15}N$, %C and %N, and the collagen yield (47–50). For Abri Peyrony, the C:N ratios and collagen yields are provided in Table S3. The C:N ratios of all samples are 3.2 which is fully in the acceptable range (between 2.9 and 3.6), and the collagen

yield is higher than 1.3 % where the acceptable limit is not less than 1% of weight for a sufficiently well preserved bone (49).

Once we established the collagen preservation, between 3 and 5mg of collagen were sent to the Mannheim AMS laboratory (Lab code: MAMS) for radiocarbon dating. The results are shown in Table S3 and Fig. S 13. All dates were corrected for a preparation background estimated from ^{14}C free bone samples, kindly provided by the ORAU, pretreated in the same way as the archaeological samples.

The uncalibrated radiocarbon dates from Levels L-3B and L-3A range from 43,890 to 37,270 ^{14}C BP.

3.3.3   14C Modeling, Calibration & Discussion

The radiocarbon dates were calibrated using OxCal 4.1 (51) and IntCal09 (15), and a Bayesian age distribution model was built. Treating Levels L-3A and L-3B as a contiguous phases resulted in a low agreement, hence judging from the radiocarbon dates these two phases must be considered contemporaneous. The final age model (Fig. S14) treats Levels L-3A and L-3B as one single phase. We obtained an OxCal agreement of 99.7%. The range calculated from the model is 47,710 to 41,130 Cal BP (68.2%) (Table S4).

Table S3. Results of AMS radiocarbon dating of seven samples of cut-marked bone from Abri Peyrony, Levels L-3A and L-3B. C:N ratios, %C and %N, and amount of collagen extracted (%Coll) refer to the >30 kDa fraction. δ13C values are reported relative to the vPDB standard and δ15N values are reported relative to the AIR standard. ◈ Indicates cut-marked bones.

Abri Peyrony code	Layer	MPI code Number	%Coll	δ13C	δ15N	%C	%N	C:N	AMS Nr.	14C Age	Err 1σ
◈AP-3770	L-3A	S-EVA 22429 II	1.3	-19.78	4.26	40.48	14.88	3.2	MAMS-14592	41510	279
◈AP-2081	L-3A	S-EVA 22436 II	1.5	-19.79	5.8	41.03	15.02	3.2	MAMS-14588	37500	181
◈AP-4036	L-3A	S-EVA 22437 II	2.0	-19.56	4.74	39.03	14.21	3.2	MAMS-14590	40440	251
◈AP-5409	L-3B	S-EVA 22439 II	1.6	-19.01	6.87	39.89	14.65	3.2	MAMS-14591	39460	234
◈AP-5332	L-3B	S-EVA 22442 I	1.7	-19.2	6.6	20.8	7.6	3.2	MAMS-14111	37270	257
◈AP-5312	L-3B	S-EVA 22444 II	2.4	-18.98	6.72	38.37	14	3.2	MAMS-14589	39880	247
◈AP-5855	L-3B	S-EVA 22445 I	2.5	-19.1	7.5	37.7	13.9	3.2	MAMS-14113	43890	476

Fig. S 13. Uncalibrated radiocarbon dates for Abri Peyrony Levels L-3A and L-3B.
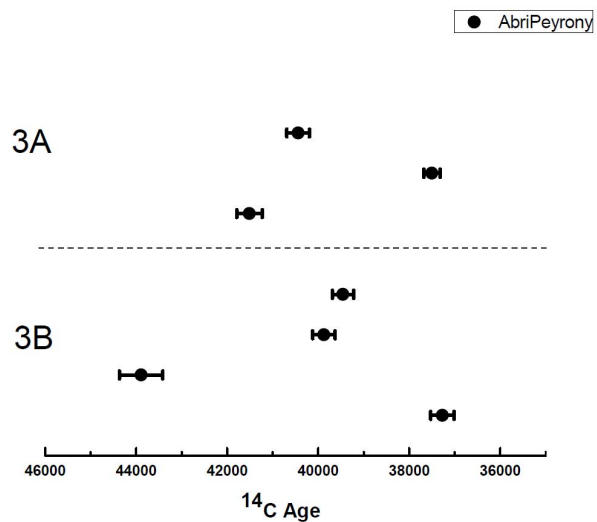
Table S4. Calibrated age ranges for the samples from Abri Peyrony as calculated by OxCal.

Abri Peyrony	Modelled (BP)			
Indices Amodel 99.9 Aoverall 99.7	from 68.2%	to 68.2%	from 95.4%	to 95.4%
Boundary End Levels L-3A+B	**42190**	**41130**	**42390**	**39280**
MAMS-14588 (37500,181)	42400	42020	42600	41840
MAMS-14590 (40440,251)	44600	44130	44870	43840
MAMS-14592 (41510,279)	45310	44760	45610	44520
MAMS-14111 (37270,257)	42320	41880	42550	41670
MAMS-14591 (39460,234)	43890	43290	44150	43050
MAMS-14589 (39880,247)	44220	43640	44430	43320
MAMS-14113 (43890,476)	46860	45890	47630	45500
Boundary Start Levels L-3A+B	**47710**	**46050**	**49580**	**45580**

Fig. S14. Calibrated ages and boundaries calculated using OxCal 4.1 and IntCal09 for archaeological Levels L-3A (Blue) and L-3B (black) at Abri Peyrony (15, 51). The gray probability area indicates calibrated age range without using prior information; the dark area is the Bayesian model result.

4 Fauna
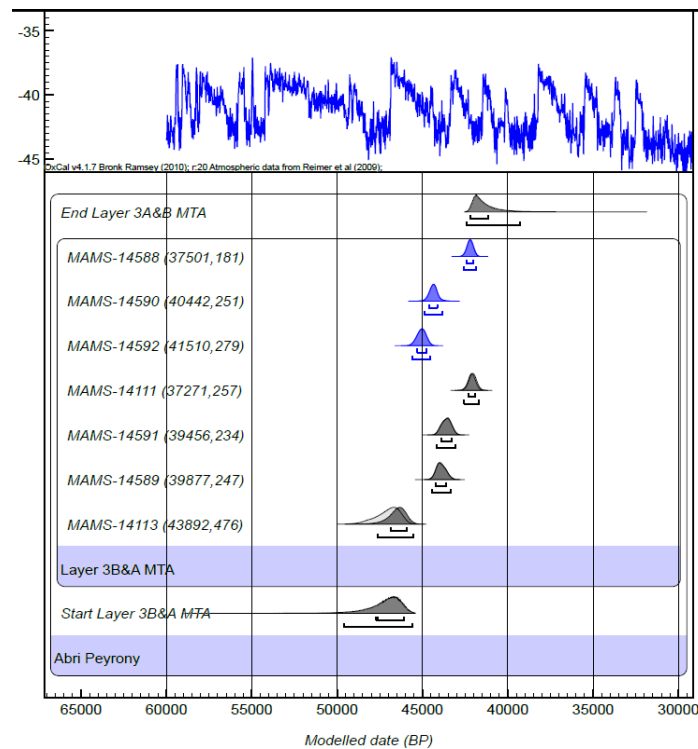
4.1 Pech-de-l'Azé I

The faunal spectrum is dominated by red deer (%NISP = 65) and bison remains (%NISP = 21) followed by horse, reindeer, and roe deer (52). Carnivore remains are represented by only two fox bone fragments.

Analysis of the bone surfaces was done under a low-angled light using a 12x hand lens. In cases where unclear anthropogenic or carnivore modifications were detected, specimens were subjected to more thorough evaluation with the aid of a 10-40x microscope. The criteria used to identify taphonomic and anthropic traces are those listed by Blumenschine *et al.* (53) and others (54, 55). Post- depositional alterations are represented in the fauna by weathering stage 1 (34%NR) and 2 (24%NR). While corrosion (<9%NR) and rounded bones (<1%NR) are infrequent, the high frequency of calcite deposit (29%NR) can limit the cortical surface examination. Carnivore modifications are rare (<1% NR). This and their low contribution to the faunal spectrum suggests that carnivores had only a limited impact on the bone fragments and probably did not notably modify the bone representation. Human modifications are present on more than 30% of the bone assemblage (Table S5). These traces combined with the abundance of the lithic artifacts, the presence of burnt bone and flint support the human origin of the fauna.

Table S3. Anthropic activity on bones from Pech-de-l'Azé I Layer 4 (N= 2632, all bones except micro-fauna). Low-confidence cases are not included here.

Bones with human modification		Cut marks		Scrapping		Retoucher		Percussion Notches		Bone flakes		Burned bones	
N	%	N	%	N	%	N	%	N	%	N	%	N	%
800	30.5%	305	11.6%	39	1.5%	15	0.6%	165	6.3%	119	4.5%	273	10.4%

4.2 Abri Peyrony Fauna

The fauna from L-3A is dominated by large bovids and horses (74% of the sample of 140 bones assigned to taxa of 267 piece-plotted bones). Cervids are present as well (16%). Fragments of only two large carnivore bones have been found. The L-3B fauna contains a much higher proportion of cervids (93% of the sample of 375 bones assigned to taxa of the 691 piece-plotted bones), and when they can be further identified to species, they are reindeer. In the current sample, only two medium carnivore remains have been identified from L-3B.

Analysis of the bone surfaces was done under a low-angled light, using a hand lens when necessary. Like Pech 1's Layer 4, human modifications are present on more than 30% of the bone assemblages (Table S6). Overall, the L-03A fauna is well preserved; only 18% of the bones show weathering stage 1, 4% were weathered to stage 2, and only two bones in stage 3, following Behrensmeyer (56) . Only one bone shows evidence of abrasion. Only three bones show evidence of acidic attack (from either carnivores or soils), and none show evidence of modification from carnivore chewing. The L-3B fauna is equally well preserved, with 12% of the specimens currently analyzed exhibiting weathering stage 1 and only 3% in stage 2, 3 or 4; six are abraded. 22% have cut marks, 10% have impact notches, but only a few are burnt (6%). Five bones are acid etched and two show carnivore damage. Carnivores appear to have played a minimal role in accumulating and impacting the assemblages. The abundance of human traces associated with lithic artifacts confirms the human origin of the faunal assemblages.

Table S6. Anthropic activity on bones from Abri Peyrony. Samples are through 2010 season.

Level	N	Bones with human modification		Cut marks		Scraping		Retoucher		Percussion Notches		Bone flakes		Burned bones	
		N	%	N	%	N	%	N	%	N	%	N	%	N	%
L-3A	266	91	34%	29	11%	5	2%	0	0%	6	2%	5	2%	55	21%
L-3B	687	250	36%	153	22%	32	5%	2	<1%	67	10%	9	1%	39	6%

5   Additional Photos and 3D PDF Models of the Bones

5.1   Photographs
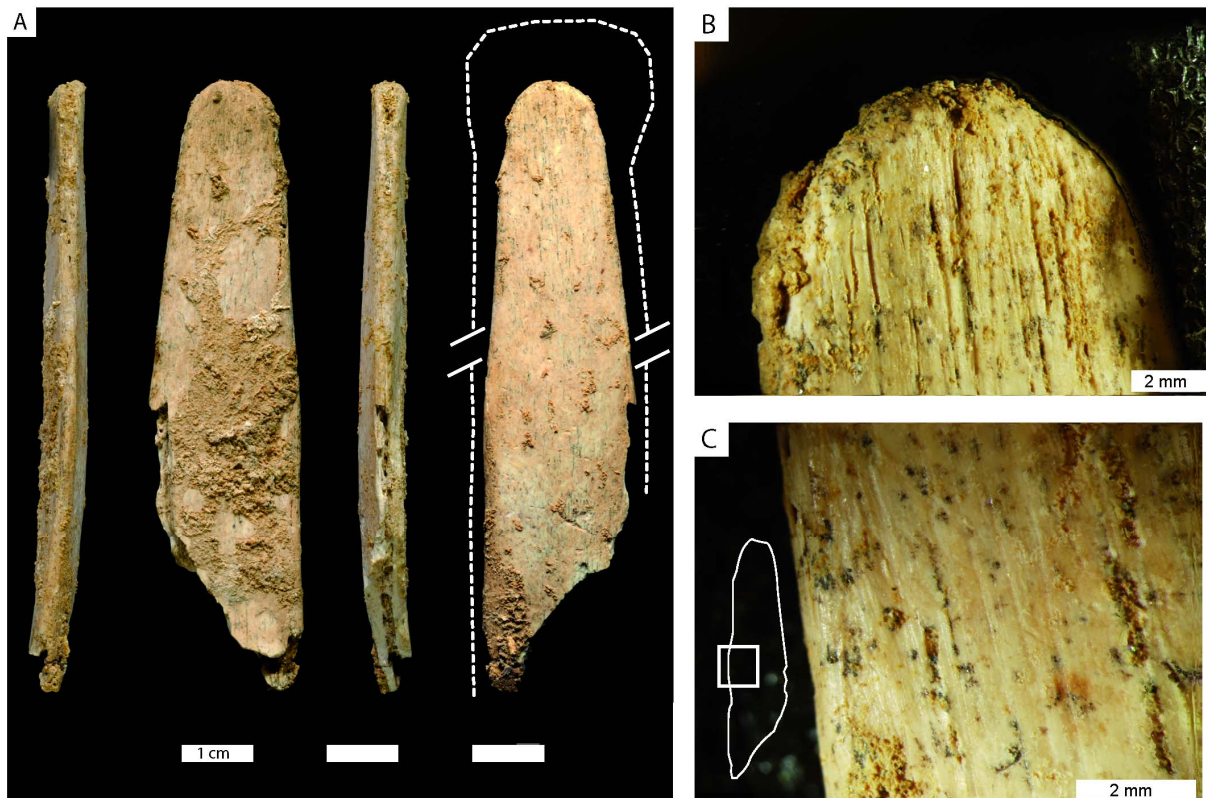

Fig. S15. AP-7839 photomicrographs. On A, the original shape of the rib, before human modification, is indicated as an interrupted dotted line. The bone measures 82.67 L x 20.12 W x 5.93 T (mm).

Fig. S16. AP-4209 photomicrographs. From left to right, cortical face, profile, and interior face. Below : alternate views of the tip (top) and base. The bone measures 21.1 L x 14.8 W x 4.8 T (mm).
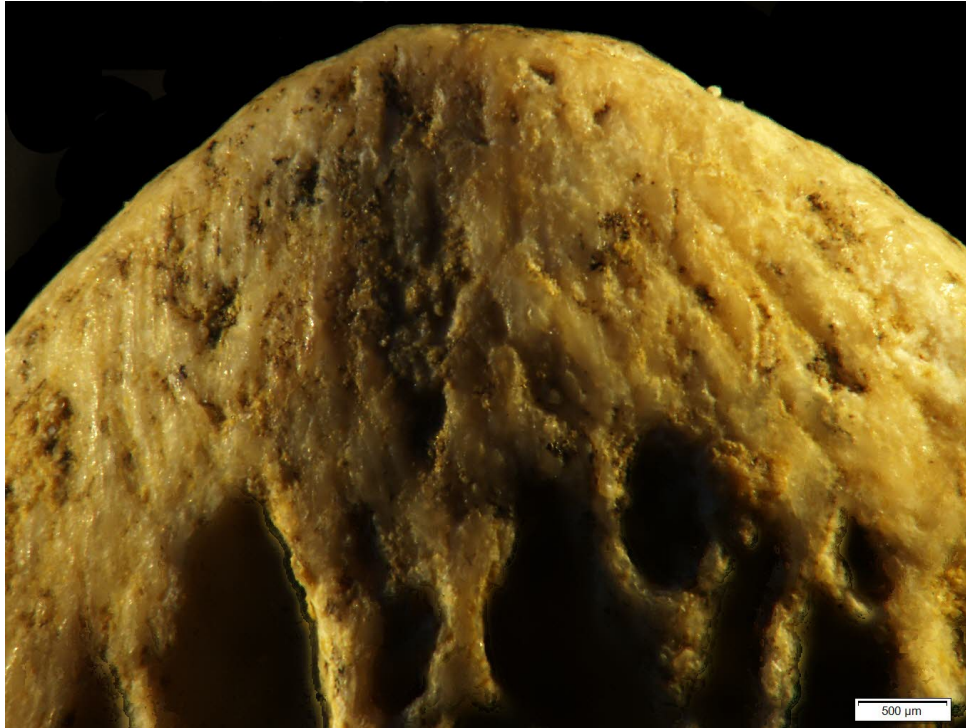
Fig. S17. AP-4209 photomicrograph of interior of the tip. Note the multiple parallel striations from the center to the left and note the two parallel deep grooves on the right and emanating from the tip.

Fig. S18. AP-4493 photomicrographs. From left to right, cortical face, profile, and interior face. The bone measures 20.9 L x 12.7 W x 3.8 T (mm).

Fig. S19. AP-4493 photomicrographs. Alternate views of the tip (top) and base.

Fig. S20. G8-1417 photomicrographs. Upper left, tip. Bottom, left to right, cortical face, profile, interior face, and profile. The bone measures 33.3 L x 16.1 W x 2.9 T.

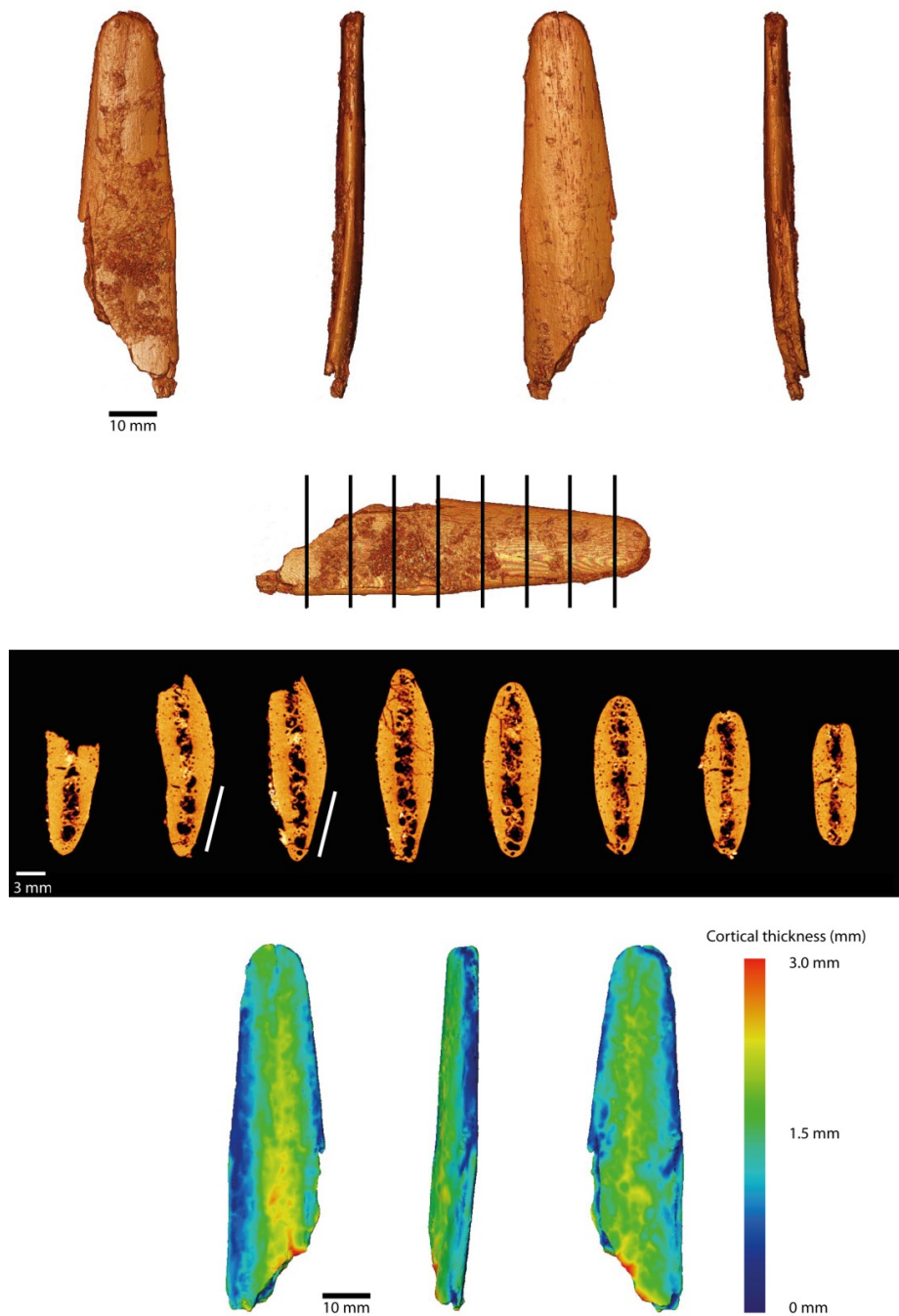Fig. S21. Sections through the scan of AP-7839 (above and center) illustrating reduction of cortical thickness and loss of cortical edges near the tip. Model of cortical bone thickness (below) again illustrating loss of cortical bone on both sides near the tip.

5.2 3D PDF Models

Interactive 3D models of all four bones are included as Supporting Information PDFs.

5.3 Methods for microtomographic scanning and surface model preparation

Specimens AP-4493 and AP-7839 were scanned on a BIR ACTIS 225/300 high resolution micro-CT scanner using the following parameters: 120kV, 120uA, exposure time 999ms, 0.225 rotation step, no filter, resolution = 0.01204 mm. Specimens AP-4209 and G8-1417 were scanned on a SkyScan 1172 with the following parameters: 100kV, 94 uA, 0.12 rotation step, 2.0mm aluminum and copper filter, resolution = 0.01344 mm.

The reconstructed image stack for each specimen was downsampled to 0.028mm in Avizo 6.3 (*resample* module using a triangle filter). A triangulated surface was generated (*isosurface* module) based on a threshold between air and bone. The surface model was resampled to 750,000 faces and was exported as in STL format. Each STL file was converted to a 3D PDF using Microsoft Office Word 2007. The STL files are included in separate Supplemental Information files. The 3D PDF files are embedded here and follow.

6 Definition of *lissoir* in Upper Paleolithic Contexts

Lissoir as a bone tool type was first described in 1861 by Lartet based on his excavations at the Aurignacian type site of Aurignac (France) as cited by Tatar (57). However, as Tatar notes in her study and review of bone tools in the early Aurignacian, despite numerous discoveries since then and several studies, the tool type remains poorly defined. Tatar (*39:67*) states that most definitions have in common an elongated, thin object with a blunted end showing a gloss that is interpreted as resulting from working the object against a soft material. This definition, however, is general enough that it can also include other types of objects including so-called spatulas which show a larger or enlarged mesio-distal end and a protuberant proximal end. Additionally, Tatar notes that so-called *brunissoirs* (burnishers) are also quite similar but are described as being thicker, more robust, and made on antler. In calling the pieces described here *lissoir*, we are following Averbouh's (2000:194 as quoted by Tatar (57)) definition as "*objet*

principalement en os, plat et allongé, caractérisé par une extrémité distale, de forme variée (ogivale, convexe ou triangulaire) dont l'orientation par rapport à l'axe longitudinal de la pièce la définit comme d'axe ou d'angle. Cette extrémité active, voire la partie active, est souvent marquée par un lustre, des facettes et des stries résultant tous de l'utilisation." While the *lissoir* shape is standardized, their size varies according to the size of the bone used as a blank. Tatar (57) then considers *brunissoirs* and spatula as sub-types of *lissoir*. *Lissoir*, as much as can be determined, are made on ribs and tend to be made on ribs split lengthwise (*39:67-69*). When they are made on split ribs, one face is cortical and the other is typically spongy bone if this bone has not been completely worn away.

7 Other potential Middle Paleolithic *lissoir* : the La Quina Bone Tool

The La Quina bone tool was found by Dr. Henri-Martin in March, 1907, during his excavation in the upper layers of Mousterian site. He published the artifact twice with precise descriptions and excellent photographs (58, 59). His work is summarized here. More recently, the upper layers of this portion of the site (the so-called *Station Amont*) have been shown to contain Mousterian of Acheulian Tradition and Denticulate Mousterian industries (60).

The bone tool is a complete, 50 cm long, object made on a bovid rib (Fig. S22). Henri-Martin attributed it to a 10th left rib. The superposition of this rib with a complete, modern bovid rib shows that 10 cm of distal extremity was removed. After removing these 10 cms, the extremity of the La Quina rib was reshaped into an ogival tip by modifications of both edges. These modifications continue some 15 cm along the edge. Again, the superposition with a modern bovid rib shows that a substantial thickness of the bone was removed from the edge as the modern rib is 4.5 cm wide while the La Quina rib is only 1cm wide (similar to the fragments reported here). As a consequence, about 1.5 cm of bone was removed on both sides of the bone

to obtain a symmetrical and smooth ogival tip. According to Henri-Martin's (59) descriptions, the distal third of the rib is polished on both faces, and the inner spongy bone is visible on both faces over the distal 4 cms. Henri-Martin (59) also writes that one edge shows a longitudinal, deep groove (*sillon*) which might be evidence of the last shaping event with a stone-tool. On the proximal end, the shape of the original rib is intact but Henri-Martin reports numerous scraping marks made with a stone tool.
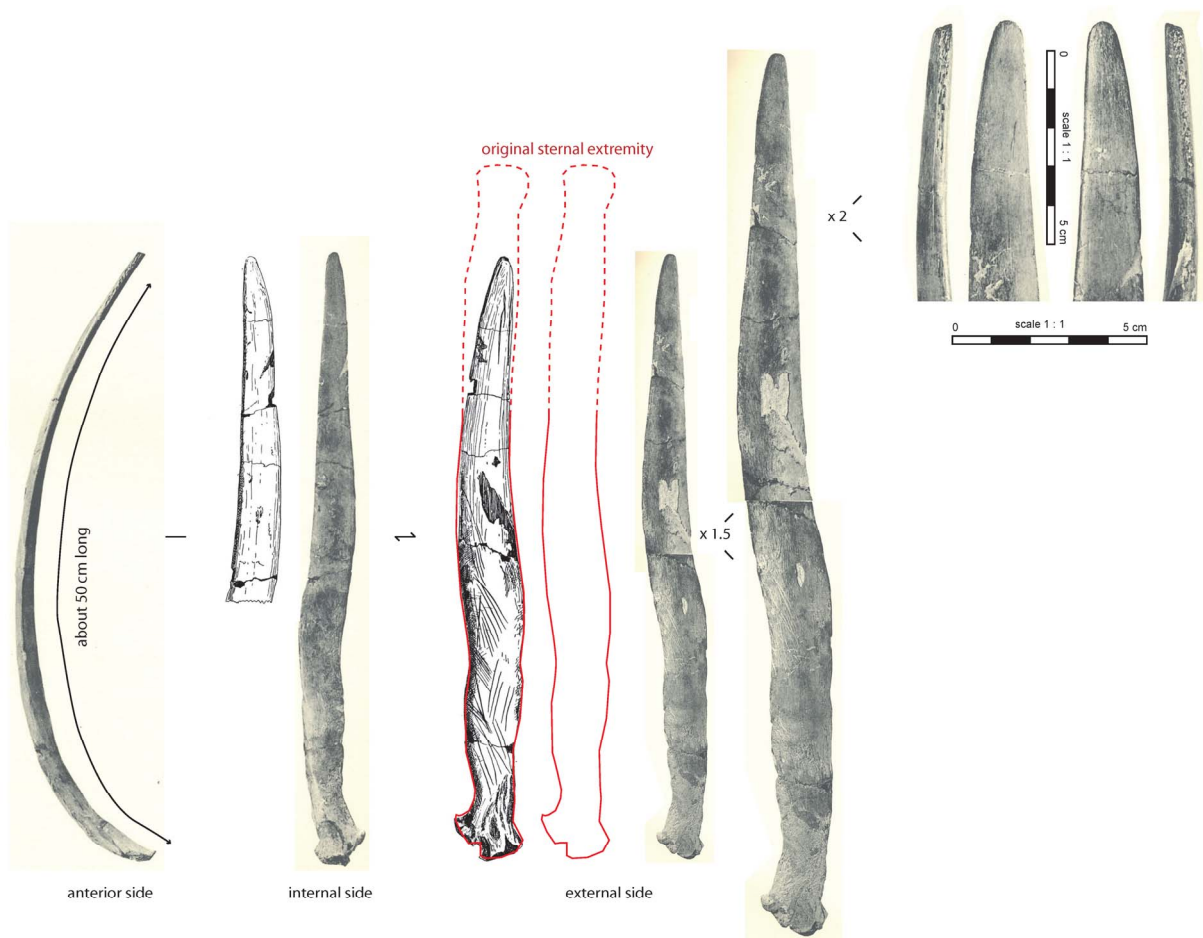

Fig. S22. La Quina bone tool. Photographs and drawings after Martin (59), pl. XXV. The contour of the original rib was drawn after the contour of a modern 10th bovid rib.

Similarities in tip morphology and polish between the La Quina bone tool and the bone tool fragments reported here are clear (Fig. S23). The La Quina bone tool may provide a model

for how the *lissoirs* reported here may have looked when complete, though the *lissoirs* reported here were more likely made from cervid bone. Aside from the species related size differences, a break in the distal portion of the La Quina tool would produce a bone very much like AP-7839. Note that the S-profile of broken ends of the three smaller *lissoir* fragments reported here suggests that the break occurred while the bone was still fresh (the other broken during excavation - though some is missing it is also clear that it was not complete like the La Quina example). Further, the orientation of the polish, particularly on AP-4209, suggests that the preserved cortical surface on each of these smaller fragments is in fact the upper side of the object that snapped off as a downward pressure was applied to the lower or contact side of the piece during use.

An on-going effort to relocate the La Quina rib for study has been unsuccessful.
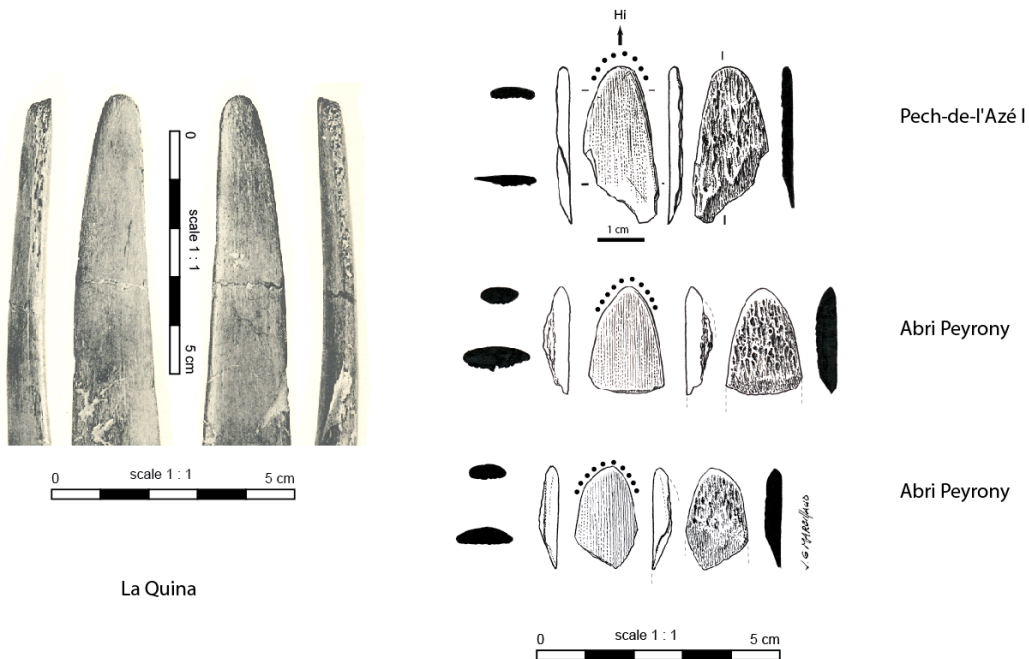

Fig. S23. Close-up of La Quina bone and the three smaller fragments from Pech-de-l'Azé I and Abri Peyrony (photo of La Quina after Martin (59), pl. XXV).

A red deer rib fragment from the Middle Paleolithic site of L'Abri de Canalette has also been interpreted as a *lissoir* (61). One end of the 12.5 cm long piece is rounded and polished and shows multiple parallel microstriations. Based on the plan view photo, the tip is more rounded and less ogival than the bones reported here, and the absence of profile and underside photos limits additional comparison. The piece is reported as currently under additional study.

8 Additional microwear information for the Pech I *lissoir*

The absence of traces on the spongy tissue, in contrast to the cortical face, suggests that the object is in fact the sagittal half of a tool that was broken during use or after abandonment. The marginal extent of microscopic traces on this artifact is certainly related to the fact that this is only the upper side of a tool. Wear resulting from hide-working can indeed be invasive on the contact side but very limited on the upper side. The macro-striations can be attributed to the presence of an abrasive.

bending fracture

section view of the bending fracture

Fig. S24. A schematic showing our reconstruction of the potential use of *lissoir* compatible with unique use-wear pattern observed on each of the *lissoir* discovered at Abri Peyrony and Pech I (redrawn after Semenov 62:178). The morphology of both ends of a *lissoir*, in oblique view and in section, after a bending fracture resulting from use is also indicated.

9 References

1. McPherron SP, Dibble HL (2002) *Using Computers in Archaeology: A Practical Guide* (McGraw Hill, New York).

2. Soressi M et al. (2008) in *Les sociétés du Paléolithique dans un Grand Sud-Ouest de la France: nouveaux gisements, nouveaux résultats, nouvelles méthodes* [Paleolithic Societies in the Greater Southwest of France: New Sites, New Results, and New Methods] (Société Préhistorique française, Mémoire XLVII), pp 95–132.

3. Lenoir M, Dibble HL (1995) in *The Middle Paleolithic site of Combe-Capelle Bas (France)* (University of Pennsylvania Museum Press, Philadelphia), pp 329–340.

4. Peyrony D (1925) Le gisement préhistorique du haut de Combe-Capelle. Moustérien de Tradition Acheuléenne [The Prehistoric Site of Haut de Combe-Capelle. Mousterian of Acheulian Tradition]. *Association Française pour l'Avancement des Sciences* 49:484–487.

5. Laville H (1973) Climatologie et chronologie du Paléolithique en Périgord : étude sédimentologique de dépôts en grottes et sous abris [Climatology and Chronology of the Paleolithic in the Périgord: Sedimentological Study of Cave and Rockshelter Deposits].

6. Texier J-P (2009) *Histoire Géologique de Sites Préhistoriques Classiques du Périgord: Une Vision Actualisée* [A Geological History of the Classic Prehistoric sites of the Périgord: An Updated View] (Éditions du Comité des travaux historiques et scientifiques, Paris).

7. Delfaud J (1975) Considération sur les directions armoricaines et varisques en Aquitaine [A Consideration of the Armoricaines and Varisques Directions in the Aquitaine]. *Bulletin de la Société Linnéenne de Bordeaux* V:27–32.

8. Soressi M, Jones HL, Rink WJ, Maureille B, Tillier A-M (2007) The Pech-de-l'Azé I Neandertal child: ESR, uranium-series, and AMS 14C dating of its MTA type B context. *Journal of Human Evolution* 52:455–466.

9. Baize D, Girard M-C (1995) *Référentiel pédologique* [Soils Reference]. *INRA* (Paris).

10. Meignen L, Goldberg P, Bar-Yosef O (2007) in *The Middle and Upper Paleolithic Archaeology of the Kebara Cave, Mt. Carmel, Israel* (Peabody Museum, Harvard University, Cambridge, MA), pp 91–122.

11. Goldberg P et al. (2012) New evidence on Neandertal use of fire: Examples from Roc de Marsal and Pech de l'Azé IV. *Quaternary International* 247:325-340.

12. Bertran P, Texier J-P (1995) in *The Middle Paleolithic Site of Combe-Capelle Bas (France)* (University Museum Press, Philadelphia), pp 179–192.

13. Stoops G (2003) *Guidelines for analysis and description of soil and regolith thin sections* (Soil Science Society of America, Madison, Wisconsin).

14. Courty M-A, Goldberg P, Macphail R (1989) *Soils and micromorphology in archaeology.* (Cambridge University Press, Cambridge).

15. Reimer PJ et al. (2009) IntCal09 and Marine09 radiocarbon age calibration curves, $0-50$ cal kBP. *Radiocarbon* 51:1111–1150.

16. Huntley DJ, Godfrey-Smith DI, Thewalt M (1985) Optical dating of sediments. *Nature* 313:105–107.

17. Aitken MJ (1998) *An introduction to optical dating: the dating of Quaternary sediments by the use of photon-stimulated luminescence* (Oxford University Press, Oxford).

18. Duller GAT (2004) Luminescence dating of Quaternary sediments: recent developments. *Journal of Quaternary Science* 19:183–192.

19. Lian OB, Roberts RG (2006) Dating the Quaternary: progress in luminescence dating of sediments. *Quaternary Science Reviews* 25:2449–2468.

20. Jacobs Z, Roberts RG (2007) Advances in optically stimulated luminescence dating of individual grains of quartz from archeological deposits. *Evolutionary Anthropolgy: Issues, News, and Reviews* 16:210–223.

21. Wintle AG (2008) Fifty years of luminescence dating. *Archaeometry* 50:276–312.

22. Wintle AG (1997) Luminescence dating: laboratory procedures and protocols. *Radiation Measurements* 27:769–817.

23. Bøtter-Jensen L, Bulur E, Duller G, Murray A (2000) Advances in luminescence instrument systems. *Radiation Measurements* 32:523–528.

24. Jacobs Z et al. (2008) Ages for the Middle Stone Age of southern Africa: Implications for human behavior and dispersal. *Science* 322:733–735.

25. Duller G (2003) Distinguishing quartz and feldspar in single grain luminescence measurements. *Radiation Measurements* 37:161–165.

26. Cunningham AC, Wallinga J (2010) Selection of integration time intervals for quartz OSL decay curves. *Quaternary Geochronology* 5:657–666.

27. Duller G (2007) Assessing the error on equivalent dose estimates derived from single aliquot regenerative dose measurements. *RN* 25:15–24.

28. Ballarini M, Wintle A, Wallinga J (2006) Spatial variation of dose rate from beta sources as measured using single grains. *Ancient TL* 24:1–7.

29. Jacobs Z, Duller GAT, Wintle AG (2006) Interpretation of single grain De distributions and calculation of De. *Radiation Measurements* 41:264–277.

30. Arnold L, Roberts R (2009) Stochastic modelling of multi-grain equivalent dose (D_e) distributions: Implications for OSL dating of sediment mixtures. *Quaternary Geochronology* 4:204–230.

31. Galbraith RF, Roberts RG, Laslett G, Yoshida H, Olley JM (1999) Optical Dating Of Single And Multiple Grains Of Quartz From Jinmium Rock Shelter, Northern Australia: Part I, Experimental Design And Statistical Models*. *Archaeometry* 41:339–364.

32. Duller G, Bøtter-Jensen L, Murray A (2000) Optical dating of single sand-sized grains of quartz: sources of variability. *Radiation Measurements* 32:453–457.

33. Bøtter-Jensen L, Mejdahl V (1988) Assessment of beta dose-rate using a GM multicounter system. *International Journal of Radiation Applications and Instrumentation. Part D. Nuclear Tracks and Radiation Measurements* 14:187–191.

34. Aitken MJ (1985) *Thermoluminescence dating* (Academic Press, London).

35. Mejdahl V (1979) Thermoluminescence dating: beta-dose attenuation in quartz grains. *Archaeometry* 21:61–72.

36. Bell WT, Zimmerman DW (1978) The effect of HF acid etching on the morphology of quartz inclusions for thermoluminescence dating. *Archaeometry* 20:63–65.

37. Rhodes E, Schwenninger J (2007) Dose rates and radioisotope concentrations in the concrete calibration blocks at Oxford. *Ancient TL* 25:5–8.

38. Mercier N, Falguères C (2007) Field gamma dose-rate measurement with a NaI (Tl) detector: re-evaluation of the "threshold" technique. *Ancient TL* 25:1–4.

39. Jones HL (2001) Electron Spin Resonance (ESR) dating of tooth enamel at three Paleolithic archaeological sites.

40. Prescott J, Hutton J (1994) Cosmic ray contributions to dose rates for luminescence and ESR dating: large depths and long-term time variations. *Radiation measurements* 23:497–500.

41. Smith M, Prescott JR, Head M (1997) Comparison of 14C and luminescence chronologies at puritjarra rock shelter, central Australia. *Quaternary Science Reviews* 16:299–320.

42. Galbraith R (2003) A simple homogeneity test for estimates of dose obtained using OSL. *Ancient TL* 21:75–77.

43. Talamo S, Richards MP (2011) A Comparison of Bone Pretreatment Methods for AMS Dating of Samples > 30,000 BP. *Radiocarbon* 53:443–449.

44. Longin R (1971) New method of collagen extraction for radiocarbon dating. *Nature* 230:241–242.

45. Brown TA, Nelson DE, Vogel JS, Southon JR (1988) Improved Collagen Extraction by Modified Longin Method. *Radiocarbon* 30:171–177.

46. Brock F, Ramsey CB, Higham T (2007) Quality assurance of ultrafiltered bone dating. *Radiocarbon* 49:187–192.

47. Schoeninger MJ, Moore KM, Murray ML, Kingston JD (1989) Detection of bone preservation in archaeological and fossil samples. *Applied Geochemistry* 4:281–292.

48. Ambrose SH (1990) Preparation and Characterization of Bone and Tooth Collagen for Isotopic Analysis. *Journal of Archaeological Science* 17:431–451.

49. Van Klinken GJ (1999) Bone Collagen Quality Indicators for Palaeodietary and Radiocarbon Measurements. *Journal of Archaeological Science* 26:687–695.

50. Hedges REM (2002) Bone diagenesis: an overview of processes. *Achaeometry* 44:319–328.

51. Ramsey CB (2009) Bayesian analysis of radiocarbon dates. *Radiocarbon* 51:337–360.

52. Rendu W (2010) Hunting behavior and Neandertal adaptability in the Late Pleistocene site of Pech-de-l'Azé I. *Journal of Archaeological Science* 37:1798–1810.

53. Blumenschine RJ, Marean CW, Capaldo SD (1996) Blind Tests of Inter-analyst Correspondence and Accuracy in the Identification of Cut Marks, Percussion Marks, and Carnivore Tooth Marks on Bone Surfaces. *Journal of Archaeological Science* 23:493 – 507.

54. Olsen SL, Shipman P (1988) Surface modification on bone: Trampling versus butchery. *Journal of Archaeological Science* 15:535–553.

55. Pickering TR, Egeland CP (2006) Experimental patterns of hammerstone percussion damage on bones: implications for inferences of carcass processing by humans. *Journal of Archaeological Science* 33:459–469.

56. Behrensmeyer AK (1978) Taphonomic and ecologic information from bone weathering. *Paleobiology* 4:150–162.

57. Tartar E (2009) De l'os à l'outil. Caractérisation technique, économique et sociale de l'utilisation de l'os à l'aurignacien ancien. Etude de trois sites : l'abri Castanet (secteurs nord et sud), Brassempouy (grotte des Hyènes et abri Dubalen) et Gatzarria [From Bone to Tool. Technical, Economic, and Social Characterization of the use of bone in the Early Aurignacian. A study of Three Sites : l'abri Castanet (sectors north and south), Brassempouy (grotte des Hyènes and abri Dubalen) and Gatzarria] (Doctoral Thesis, Université de Paris I, Paris).

58. Martin H (1907) Présentation d'ossements utilisés de l'époque moustérienne [Presentation of the Utilized Bones from the Mousterian Period]. *Bulletin de la Société Préhistorique Française* 4:269–277.

59. Martin H (1909) *Recherches sur l'Evolution du Moustérien dans le Gisement de La Quina (Charente) Vol.1, Fasc. 2. Ossements Utilisés* [Research into Mousterian Evolution in the site of La Quina (Charente) Vol. 1, Fasc. 2. Utilized Bones] (Schleicher Frères, Paris).

60. Debenath A, Jelinek AJ (1998) Nouvelles fouilles à La Quina (Charente): Résultats préliminaires [New Excavations at La Quina (Charente) : Preliminary Results]. *Gallia. Préhistoire* 40:29–74.

61. Patou-Mathis M (1993) in *L'abri des Canalettes: Un habitat moustérien sur les grands Causses (Nant, Aveyron)* [L'Abri des Canalettes : A Mousterian site in the Causses Region (Nant, Aveyron)] (Centre National de la Recherche Scientifique, Paris), pp 199–237.

62. Semenov SA (1964) *Prehistoric technology* (Cory, Adams & Mackay).

10 Author contributions

M.S. directs the Pech I project. Pech I lithic analysis and excavation by M.S., use-wear analyses by Y.M, zooarcheology and taphonomy by W.R , geology by J.-P.T., combustion feature micromorphology by P.G., and OSL dating by Z.J. W.R. recognized the bone-tool. AP lithic analysis and excavation by S.P.M., M.L., and T.D., zooarchaeology by T.S. and N.M., geology by C.M., and radiocarbon dating by S.T. and M.R. Peng Fei, Will Archer, and N.M. found the AP bone-tools. M.M.S. scanned the bone-tools, created 3D graphics, and prepared on-line 3D data set. M.S. and S.P.M. wrote the paper with contributions and discussions with all authors.